ISPRS Journal of Photogrammetry and Remote Sensing 164 (2020) 184–199

Contents lists available at ScienceDirect

ISPRS Journal of Photogrammetry and Remote Sensing

journal homepage: www.elsevier.com/locate/isprsjprs

Correction of amplitude scintillation effect in fully polarimetric SAR coherency matrix data

Shradha Mohanty[a,*], Unmesh Khati[a], Gulab Singh[a], E. Chandrasekhar[b]

[a] Centre of Studies in Resources Engineering, Indian Institute of Technology Bombay, India
[b] Department of Earth Sciences, Indian Institute of Technology Bombay, India

ARTICLE INFO

Keywords:
ALOS-2/PALSAR-2
Amplitude scintillations
Coherency matrix
Correction
Discrete wavelet transform (DWT)
Fast Fourier transform (FFT)
Ionosphere
L-band
Model-based decomposition
POLSAR

ABSTRACT

In this paper, we investigate the correction of ionospheric amplitude scintillations appearing as image artifacts in low frequency synthetic aperture radar (SAR) data. A method has been proposed to separate amplitude and phase components of fully polarimetric SAR (POLSAR) coherency matrix [T], and then implement a combination of multi-level, two-dimensional Discrete Wavelet Transform and Fast Fourier Transform (DWT-FFT) to correct the amplitude scintillation-induced stripes in [T] matrix. In the methodology, [T] is decomposed into component matrices of amplitude and relative phases. To the amplitude [T] matrix, a combination of 2-D DWT is performed, using the Haar wavelet, followed by a non-linear 2-D FFT correction strategy to remove amplitude scintillation stripes. Using DWT, each amplitude [T] matrix element is decomposed into low- and high-frequency components known as approximate and detailed coefficients respectively. On applying a 2-D FFT on the detailed coefficients, amplitude scintillation-induced stripes are easily identified in the frequency spectrum and then removed using 2-D FFT correction strategy of averaging-post-thresholding. The proposed method is tested on the [T] matrix of several POLSAR datasets acquired from Advanced Land Observation Satellite/Phased Array type L-band synthetic aperture radar (ALOS/PALSAR) and Advanced Land Observation Satellite-2/Phased Array type L-band synthetic aperture radar-2 (ALOS-2/PALSAR-2) satellites. The performance of the correction technique is analysed both, qualitatively and quantitatively. While improvements in the post-correction datasets are visually observed, a supervised Wishart classification also performed on the [T] matrices of undisturbed (reference), disturbed and corrected data indicates significant increase in overall accuracy (OA) and kappa coefficient ($\hat{k}$) parameters. The classification accuracies of the disturbed data (OA = 69.31%, $\hat{k}=0.54$) improved to OA = 76.49%, $\hat{k}=0.68$ after applying the proposed correction approach, which is comparable to the reference data values (OA = 81.57%, $\hat{k}=0.71$). The proposed method performs significantly better than the existing technique of a simple 2-D FFT approach (OA = 73.49%, $\hat{k}=0.62$). The contribution of dominant scattering powers, obtained from the seven-component scattering power decomposition of POLSAR coherency matrix (7SD) model, also demonstrates post-correction improvements. The dominant scattering power for targets increased by ~3–9% using the proposed approach, shows an improvement of ~3% over the existing 2-D FFT technique.

1. Introduction

Ever since the first airborne sensor with quad-polarimetric capability was flown (vanZyl et al., 1987), the remote sensing community has valued fully polarimetric synthetic aperture radar (POLSAR) data obtained from SAR over optical datasets. Cloud penetration, day-night coverage, all-weather capability and sensitivity to target's geometry and dielectric properties provide complimentary capability to SAR sensors over their optical counterparts. However, spaceborne POLSAR data are affected by numerous radiometric artifacts like range/azimuth ambiguity (Wang et al., 2018), target ghosting due to errors in Doppler frequency estimation, banding, scalloping (Shimada, 2009), and geometric errors (Jiang et al., 2016). Such errors affect SAR image processing and identification of targets, thereby reducing their applicability. For low frequency (P- and L-band) SAR data, one such imaging artifact is the stripes/streaks along the azimuth (satellite's flight) direction caused by the interaction of radar signal with large electron density irregularities in the ionosphere. This phenomenon is called as

* Corresponding author.
E-mail address: shradha_mohanty@iitb.ac.in (S. Mohanty).

https://doi.org/10.1016/j.isprsjprs.2020.04.005
Received 20 September 2019; Received in revised form 7 April 2020; Accepted 10 April 2020

ionospheric scintillation, and is defined as sudden and rapid modulations of the amplitude and/or phase of the signal waveform due to such electron density irregularities (Mohanty et al., 2018). They are of two types: amplitude scintillations that appear as strong stripes/streaks in the azimuth direction of low frequency SAR data acquired over lower latitudes magnetic equatorial region, and phase scintillations that are mostly observed at higher latitudes, near polar caps and auroral regions, resulting in reduced image contrast and blurring. The scintillation phenomenon not only degrades the visual interpretation of low frequency SAR data (Shimada et al., 2008) but also hampers the amplitude and phase of the backscatter signal (Belcher and Rogers, 2009; Belcher and Cannon, 2014).

Imaging artifacts similar to amplitude scintillation stripes are also observed in several multi-detector optical imaging sensor systems, for example Landsat Thematic Mapper (TM), MultiSpectral Scanner (MSS) and Moderate Resolution Imaging Spectrometer (MODIS) (Rakwatin et al., 2007; Carfantan and Idier, 2010). Such artifacts not only degrade the visual image quality, but also affect subsequent use of such datasets in applications such as image classification, segmentation, and information extraction. Nevertheless, correction strategies including image decomposition (Chang et al., 2016; Chen et al., 2017), statistical matching (Horn and Woodham, 1979; Gadallah et al., 2000), and digital filtering (Chen et al., 2003) have been developed for the removal of horizontal, vertical, and oblique stripes in remote sensing data (Chang et al., 2016). While understanding the complexity of interaction of low frequency SAR signal with the ionosphere, we are interested in correcting for the amplitude scintillation stripes in them. This is important especially for the currently operating L-band Advanced Land Observation Satellite-2/Phased Array type L-band Synthetic Aperture Radar-2 (ALOS-2/PALSAR-2) (Mohanty et al., 2018) and future missions like NISAR (NASA-ISRO SAR in S- and L- band) (Pi, 2015; Meyer and Agram, 2017) and BIOMASS (P-band) (Rogers et al., 2014). Keeping in mind the changing dynamics of the ionosphere as well as the absence of a physical model for correction of the amplitude scintillation stripes, we attempt its corrections from an image processing and restoration perspective to improve POLSAR data quality and its interpretation for several applications.

Although several effective destriping techniques including Fourier transforms (FT) (Liu, 2006), and wavelet transform (WT) (Torres and Infante, 2001; Chen et al., 2006) are established for optical remote sensing data, very limited approaches have been tested with SAR data (Roth et al., 2010; Roth et al., 2012; Mohanty and Singh, 2019). In a recent study, Fast Fourier Transform (FFT) technique-based linear and non-linear correction strategies are applied on the scattering power decomposition images of L-band POLSAR data affected by amplitude scintillation stripes (Mohanty and Singh, 2019). This technique assumed that the scintillation stripes appear as periodic noises, such that in the frequency domain their signatures appeared as isolated bright features compared to the low frequency of the background terrain, thus making their identification and correction easier. Although FFT approach is easy and straightforward, temporal localization (i.e., maximum concentration of the signal in time domain) of the frequency components cannot be identified with it. Further, the issues of accurately correcting the stripes from the scattering power images of the scintillation-affected data and optimally preserving the original data and other structures were not completely addressed by the FFT approach (Mohanty and Singh, 2019).

For non-periodic stripes, or stripes that have frequencies matching with structural information, FFT based methods resulted in either inclusion of ringing artifacts (Roth et al., 2012) or removal of information from the corrected image (Mohanty and Singh, 2019). While results from the wavelet-based approach are associated with notable loss of structural information (Torres and Infante, 2001), the authors agree that image transformation techniques such as FFT and WT, when individually used, might produce desirable results in many cases. Yet, all conditions for accurately correcting the stripe artifacts are not satisfied by them. In this regard, combination of image transformation techniques may allow a strict separation between the noise and original image features, thus improving the correction of artifacts and simultaneously retaining original image information (Deergha Rao et al., 2001; Münch et al., 2009; Pande-Chhetri and Abd-Elrahman, 2011). Combination of image transformation techniques provide the consequent methodology to isolate scintillation stripes from the background information. This enables precise sorting of the frequencies corresponding to the stripes into subgroups for accurate correction. For example, FFT approach with a Gaussian function and Discrete Wavelet Transform (DWT) with Daubechies wavelet functions were combined to remove horizontal and vertical artifacts in multi-detector imaging systems (Münch et al., 2009).

POLSAR coherency matrix [T] serves as a key parameter in polarimetric data analysis for qualitative and quantitative information about the scattering behavior (Fung and Chen, 2010; Moreira et al., 2013). Furthermore, [T] matrix also serves as an input for several polarimetric applications for example, incoherent target decomposition models (Yamaguchi et al., 2005) and target classification (Lee et al., 2001). This increases the applications of [T] matrix to the wide gamut of studies, such as biosphere, cryosphere, hydrosphere, and atmosphere (Yang et al., 2015). Since [T] matrix has composite elements of amplitudes (magnitude) and relative phases, currently there is no methodology available, which can be implemented to correct the amplitude scintillation artifacts in fully polarimetric relative phase [T] matrix elements. In the absence of any such correction strategy/methodology, development of an effective procedure for the correction of ionospheric amplitude scintillation effects in [T] matrix data is an urgent need of hour. In this paper, a correction method has been proposed by decomposing [T] matrix into amplitude and relative phase components matrices and by combining multi-level DWT using Haar wavelet function with a non-linear (averaging-post-thresholding strategy) FFT approach to remove amplitude scintillation-induced stripes in [T] matrix. The proposed approach is applied on L-band fully polarimetric ALOS/PALSAR and ALOS-2/PALSAR-2 datasets. To quantify the performance of the proposed method for stripe correction, we apply supervised Wishart classification technique (Lee and Grunes, 1994) on [T] matrices of disturbed data and corrected data, and compare the results and classification accuracies with the reference data. Potential of the proposed approach is also tested by applying the latest physical scattering mechanism-based seven-component scattering power decomposition of the POLSAR coherency matrix (7SD) model (Singh et al., 2019) on [T] matrices of reference data, disturbed data and corrected data. The mean scattering power values derived from corrected [T] matrix are compared with the mean scattering power values obtained from reference and disturbed datasets to demonstrate the improvement and efficacy of the proposed method.

The rest of the paper is organized as follows. Section 2 describes the list of POLSAR data affected by amplitude scintillations that have been used in this study. The preprocessing steps prior to the stripe correction are also included in the section. Methodology adopted in correcting the amplitude scintillation affected [T] matrix data and the subsequent analyses performed on them are elaborated in Section 3. Section 4 discusses the results obtained from this study. The paper is summarized and concluded in Section 5 with a brief discussion on the prospects of wavelets and FFT in similar future research.

2. POLSAR datasets and preprocessing

Spaceborne POLSAR data are acquired from ALOS/PALSAR and its successor ALOS-2/PALSAR-2 are used. The sensors for both satellites operate at 1.2 GHz in L-band frequency. A pair of data is acquired for each scene, where one dataset was affected by ionospheric amplitude scintillation and the other by relatively low or negligible scintillation. Details of the datasets used are summarized in Table 1.

Five pairs of fully-polarimetric, level 1.1 single-look complex (SLC) ALOS-2/PALSAR-2 datasets over India and one pair of ALOS/PALSAR

Table 1
Summary of POLSAR datasets utilized in the study.

Scene No./ Location	Satellite/ Sensor	Scene ID	Date of Acquisition	Ionospheric Condition	Mean Faraday Rotation Angle (^{o})
Scene 1/ India	ALOS-2/ PALSAR-2	ALOS2044900310	2015-03-23	Disturbed	3.47
		ALOS2131840310	2016-10-31	Reference	0.034
Scene 2/ India	ALOS-2/ PALSAR-2	ALOS2044900270	2015-03-23	Disturbed	2.79
		ALOS2131840270	2016-10-31	Reference	0.055
Scene 3/ India	ALOS-2/ PALSAR-2	ALOS2044900250	2015-03-23	Disturbed	2.51
		ALOS2131840250	2016-10-31	Reference	0.003
Scene 4/ India	ALOS-2/ PALSAR-2	ALOS2044900290	2015-03-23	Disturbed	2.96
		ALOS2131840290	2016-10-31	Reference	0.056
Scene 5/ India	ALOS-2/ PALSAR-2	ALOS2044900340	2015-03-23	Disturbed	5.36
		ALOS2131840340	2016-10-31	Reference	0.003
Scene 6/ Brazil	ALOS/ PALSAR	ALPSRP256737070	2010-11-19	Disturbed	0.55
		ALPSRP276867070	2011-04-06	Reference	0.017

over a part of Amazon forest, Brazil are utilized for the study. ALOS-2/PALSAR-2 has azimuth and range resolution of 5.1 m and 4.3 m respectively, while for ALOS/PALSAR the resolution is 23 m and 4 m. Swaths of the datasets are about 30–50 km in the range and 70 km along the azimuth direction. The datasets acquired on disturbed days are affected by azimuthal stripes due to strong amplitude scintillations and datasets corresponding to reference days are free from any stripes (Mohanty et al., 2018). Over India, the ALOS-2/PALSAR-2 datasets acquired on March 23, 2015 (disturbed day) were affected by amplitude scintillations, whereas those acquired on October 31, 2016 (reference day) were free from scintillation activity. The ALOS/PALSAR datasets over Amazon forest were acquired on November 19, 2010 (disturbed day) and April 06, 2011 (reference day).

In addition to ionospheric scintillations, the presence of background total electron content (TEC) also affects the propagation of SAR signal. For a linearly polarized SAR signal, the TEC changes the orientation of signal polarization. This effect is called as Faraday rotation (FR) (Bickel and Bates, 1965). Prior to any correction of amplitude scintillation stripes, POLSAR scattering matrix [S] data are first corrected for FR. The FR angle (FRA) for the datasets are estimated using the Bickel and Bates (1965) method. For fully polarimetric SAR data, this error can also be corrected using the algorithm explained by Freeman (2004), Meyer and Nicoll (2008). Mean FRA for the individual datasets are also reported in Table 1.

Post FR correction, the [S] matrix is converted into second order relative phase coherency matrix [T] using Pauli target vector k_P (Lee and Pottier, 2009). The k_P vector is represented in terms of [S] matrix elements and is further used to derive the [T] matrix as given below.

$$k_p = \frac{1}{\sqrt{2}}\begin{bmatrix} S_{HH}+S_{VV} \\ S_{HH}-S_{VV} \\ 2S_{HV}\end{bmatrix} = \begin{bmatrix} k_1 \\ k_2 \\ k_3 \end{bmatrix} \tag{1a}$$

$$\langle [T] \rangle = \langle k_p k_p^{\dagger} \rangle = \begin{bmatrix} \langle |k_1|^2 \rangle & \langle k_1 k_2^* \rangle & \langle k_1 k_3^* \rangle \\ \langle k_2 k_1^* \rangle & \langle |k_2|^2 \rangle & \langle k_2 k_3^* \rangle \\ \langle k_3 k_1^* \rangle & \langle k_3 k_2^* \rangle & \langle |k_3|^2 \rangle \end{bmatrix} = \begin{bmatrix} T_{11} & T_{12} & T_{13} \\ T_{21} & T_{22} & T_{23} \\ T_{31} & T_{32} & T_{33} \end{bmatrix} \tag{1b}$$

where, $*$ indicates the complex conjugation, $\dagger$ denotes the complex conjugation and transposition, and $\langle ... \rangle$ indicates the spatial ensemble averaging, which is obtained using the multilook factors in the azimuth and range directions. The [T] matrices generated for reference and disturbed days' datasets are represented as $[T]_{reference}$ and $[T]_{disturbed}$ respectively. The preprocessing step is graphically explained in Fig. 1.

For ALOS/PALSAR data the multilook factor is 12 × 2 (azimuth × range) representing a spatial extent of 60 m × 60 m (azimuth × range)

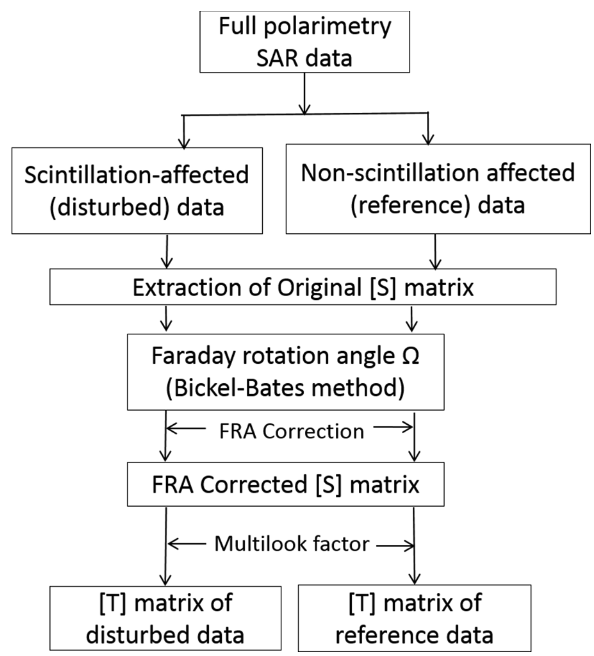

Fig. 1. Flowchart demonstrating the data preprocessing steps: Faraday rotation angle estimation, its correction in [S] matrix and subsequent [T] matrix generation.

on the ground and for ALOS-2/PALSAR-2, it is 9 × 5 (azimuth × range) representing a spatial extent of 47.7 m × 43.5 m (azimuth × range) on the ground. The incident angle calculated at the scene centres for ALOS/PALSAR data is 21.5^o and for ALOS-2/PALSAR-2 datasets is 30.85^o. The Pauli RGB color composites (red = ($S_{HH} - S_{VV}$), green = ($2S_{HV}$), and blue = ($S_{HH} + S_{VV}$)) are generated from [T] matrices of ALOS/PALSAR and ALOS-2/PALSAR-2 datasets detailed in Table 1 on days with different ionospheric activity and shown in Fig. 2. The yellow rectangles indicate the smaller subsets selected from each scene that are utilized for subsequent analyses.

3. Methodology for amplitude scintillation stripes correction from POLSAR [T] matrix

The correction approach for amplitude scintillation-induced stripes in POLSAR [T] matrix data is developed by decomposing [T] into magnitude and relative phase matrix components, and implementing a

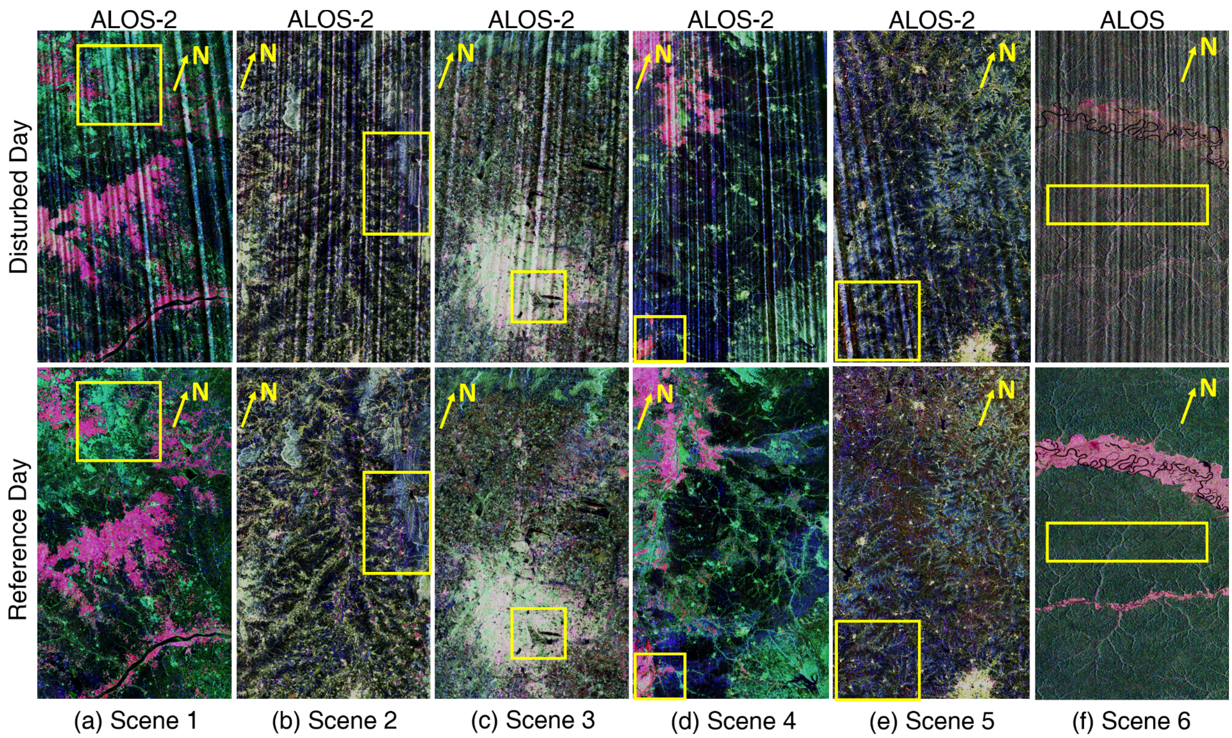

Fig. 2. Pauli RGB color composite (Red = $S_{HH} - S_{VV}$, Green = $2S_{HV}$, and Blue = $S_{HH} + S_{VV}$) of ALOS-2/PALSAR-2 and ALOS/PALSAR scenes detailed in Table 1 acquired on days with different ionospheric activity: disturbed day (top row), and reference day (bottom row). (a) Scene 1 to (e) Scene 5: data acquired over India on March 23, 2015 (top) and October 31, 2016 (bottom), (f) Scene 6: data acquired over Amazon forest, Brazil on November 19, 2010 (top) and April 06, 2011 (bottom). The yellow rectangles indicate the subsets selected for subsequent analyses. The radar look direction is from left to right in all images. (For interpretation of the references to colour in this figure legend, the reader is referred to the web version of this article.)

mixed DWT-FFT technique. The correction methodology is broadly classified into three parts; decomposition (into magnitude and relative phases), implementation of the proposed approach for correction of [T] matrix, and finally post-processing evaluation of the corrected data. Elaborate explanations of the individual procedures are given below.

3.1. Decomposition of [T] into magnitude and relative phase matrices

The manifestation of amplitude scintillation stripes in the POLSAR data is translated from the [S] matrix to the second order [T] matrix. Advantage of using the [T] is its applicability in several POLSAR methods, and that it can be inter-converted into covariance matrix [C] and Kennaugh matrix [K] (Lee and Pottier, 2009). Further, [T] matrix is directly related to the physical properties of the target that helps in interpretation. It can be decomposed into scattering powers using decomposition models and also classified using techniques such as supervised Wishart classification. Hence, it is important to correct the [T] matrix of POLSAR data affected by amplitude scintillations.

[T] matrix consists of nine independent (six real, and three imaginary) parameters. The main diagonal elements T_{11}, T_{22}, and T_{33} are real magnitude data, while the upper off-diagonal elements T_{12}, T_{13}, and T_{23} have both amplitude and phase information. However, the phase contained in them is the relative phase (or inter-phase) i.e., $\phi_{T_{12}}$, $\phi_{T_{13}}$, $\phi_{T_{23}}$. The lower diagonal elements of [T] are the complex conjugate of the upper diagonal elements. Polarization scintillation, i.e., fluctuations of phases and their coupling with each other, is extremely small for radio waves. Hence, at low-frequencies of P- and L-band, the phase fluctuations due to small-scale irregularity structures producing scintillations are same at all polarizations (Lee et al., 1982; Wheelon, 2003). As a result, their effect on the relative phase is negligible. Since [T] contains both magnitude and phase information, amplitude scintillation corrections cannot be implemented directly. These rationales are taken into account to express [T] as the product of amplitudes and relative phases for amplitude scintillation correction as given below, where 'o' denotes the Hadamard product.

$$[T]\begin{bmatrix} T_{11} & T_{12} & T_{13} \\ T_{21} & T_{22} & T_{23} \\ T_{31} & T_{32} & T_{33} \end{bmatrix} = \begin{bmatrix} |T_{11}|\ e^{j0} & |T_{12}|\ e^{j\phi_{T12}} & |T_{13}|\ e^{j\phi_{T13}} \\ |T_{21}|\ e^{-j\phi_{T12}} & |T_{22}|\ e^{j0} & |T_{23}|\ e^{j\phi_{T23}} \\ |T_{31}|\ e^{-j\phi_{T13}} & |T_{32}|\ e^{-j\phi_{T23}} & |T_{33}|\ e^{j0} \end{bmatrix}$$
$$= \begin{bmatrix} |T_{11}| & |T_{12}| & |T_{13}| \\ |T_{21}| & |T_{22}| & |T_{23}| \\ |T_{31}| & |T_{32}| & |T_{33}| \end{bmatrix} \mathrm{o} \begin{bmatrix} e^{j0} & e^{j\phi_{T12}} & e^{j\phi_{T13}} \\ e^{-j\phi_{T12}} & e^{j0} & e^{j\phi_{T23}} \\ e^{-j\phi_{T13}} & e^{-j\phi_{T23}} & e^{j0} \end{bmatrix}$$
$$= [T]_{amplitude} \quad \mathrm{o} \quad [T]_{phase} \tag{2}$$

The proposed stripe correction algorithm is applied on the $[T]_{amplitude}$ (magnitudes only) and not the relative phase $[T]_{phase}$ matrix because the effect of amplitude scintillations on the relative phases is negligible. The amplitude scintillation-induced stripes are considered to be multiplicative in nature and their correction/denoising is basically the estimation of the backscatter from the background terrain (Carrano et al., 2012). Consequently, a natural logarithm of the data separates the noise from the background information (Roth et al., 2010; Roth et al., 2012), thus enabling the easier identification and correction of the stripes. Therefore, input to the proposed approach is the natural logarithm of magnitude matrix $[T]_{amplitude}$. Details of the proposed approach is explained in the next subsection.

3.2. Proposed DWT-FFT mixed approach

Image transformations techniques, such as FFT and WT are used to represent key features of an image that are difficult to discern in the spatial domain (Torres and Infante, 2001). Several authors have utilized this property of FFT to clearly segregate low- and high-frequency components for noise suppression in remote sensing images (Watson, 1993; Rakwatin et al., 2007; Carfantan and Idier, 2010). However, time localization of signal is not possible using FFT only. Furthermore, 'windowed

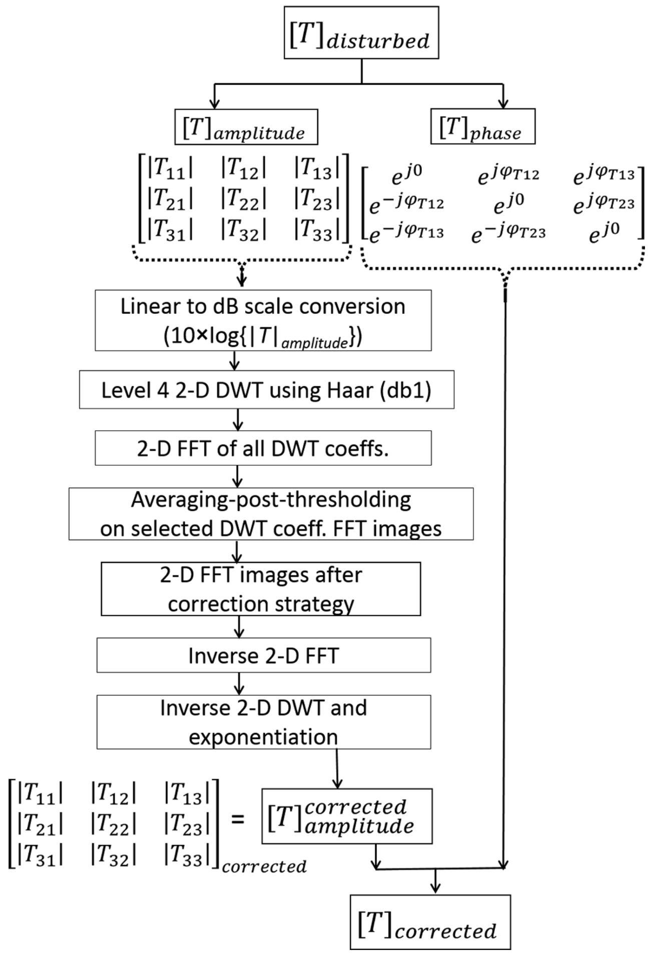

Fig. 3. Flowchart of the proposed amplitude scintillation stripe correction method implemented on [T] matrix using combination of multi-level (Level 4) 2-D DWT and non-linear 2-D FFT strategy.

Fourier transform' (WFT), which is adaptable to a simultaneous localization of the signal in time and frequency is limited by the fixed dimensions of these localizations (Ogden, 1997). Previously mentioned issues with FFT and WFT are resolved with the introduction of wavelets that automatically adapt to the time–frequency localization and signal translation and dilation (Daubechies, 1990). This property of wavelets imparts it a *'spatial adaptivity'*, which is extensively utilized in identifying sharp spikes and discontinuities in functions, and their derivatives (Ogden, 1997; Chandrasekhar et al., 2013). Such applications are frequently observed in problems of noise removal, data compression, and in identifying breakdown points, trends, and self-similarity. Furthermore, wavelets serve as prominent examples of multi-level models that are easy to switch between different levels of details or resolutions.

Although the Fourier and wavelet transforms individually have proven their competence in digital filtering domain applications, the latter is a more powerful tool compared to the FT, owing to their ability to describe varied signals in both time and frequency domains simultaneously (Karim et al., 2011). Furthermore, wavelets perform better than FT in analyzing non stationary remote sensing data (Ranchin and Wald, 1993; Meher et al., 2010), while FT provides the best results in analysing signals generated from stationary and linear time-invariant systems (Mallat, 1999). However, a combination of both these techniques is better suited than the individual methods (Münch et al., 2009; Pande-Chhetri and Abd-Elrahman, 2011). In this paper, therefore, we have adopted a combination of multi-level DWT along with the FFT technique to remove amplitude scintillation stripes induced in POLSAR data.

Let $f(x, y)$ represent the POLSAR backscatter image, with x and y representing the azimuth and slant range pixel coordinates respectively of the [T] element data. The amplitude of scintillation affected POLSAR [T] matrix elements are composed of several frequencies contributed by the background terrain as well as the stripes. The wavelet function $\psi(x, y)$ (since the image is a two-dimensional signal) decomposes the image $f(x, y)$ into one low frequency approximate coefficient A and three high frequency detailed coefficients, D_1, D_2, D_3 representing the horizontal, vertical, and diagonal components, respectively. Multi-level wavelet further decomposes the approximate coefficient into coarser frequency resolutions such that no high frequency components corresponding to the amplitude scintillation stripes are present in A. Applying FFT on the individual multi-level wavelet coefficients $(A, D_1, D_2, D_3)^i$, where (i = level of wavelet decomposition), we can identify the distribution of frequency components in the spectrum. Depending on the orientation of the scintillation stripes in the original intensity image, they appear as bright isolated features in the FFT spectra of the corresponding detailed coefficients. These high frequencies can be masked and/or removed, thus correcting the data.

In the paper, we have modified the two most important components of the mixed DWT-FFT approach, i.e., the DWT function and the filter used in the FFT to improve the correction results. While a simple Haar wavelet (also known as db1 wavelet) serves as the wavelet function, the

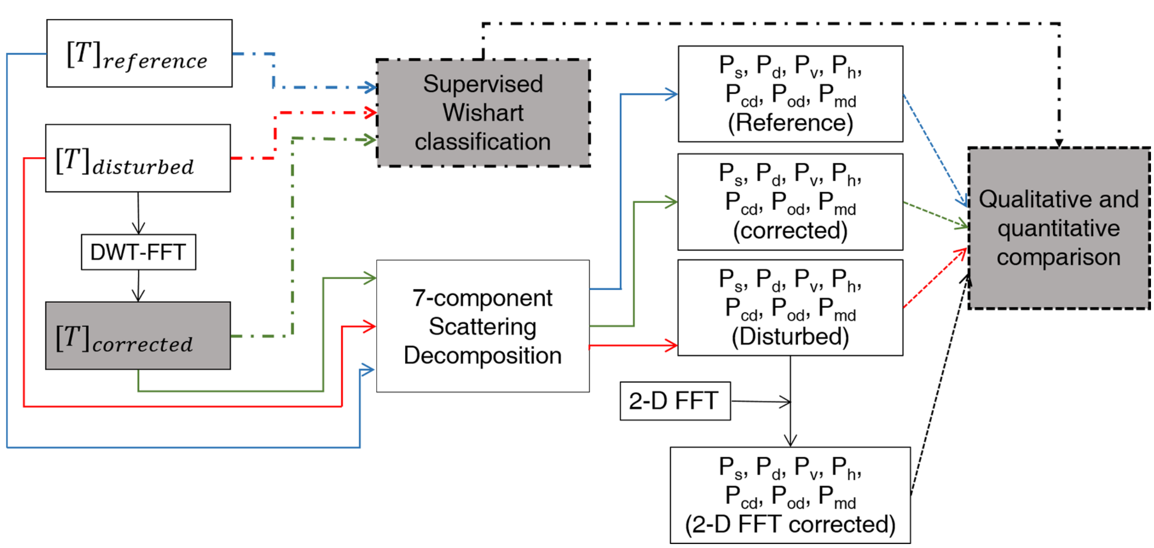

Fig. 4. Summary of the different comparative analyses performed the [T] matrix of POLSAR data corrected by the proposed mixed DWT-FFT approach.

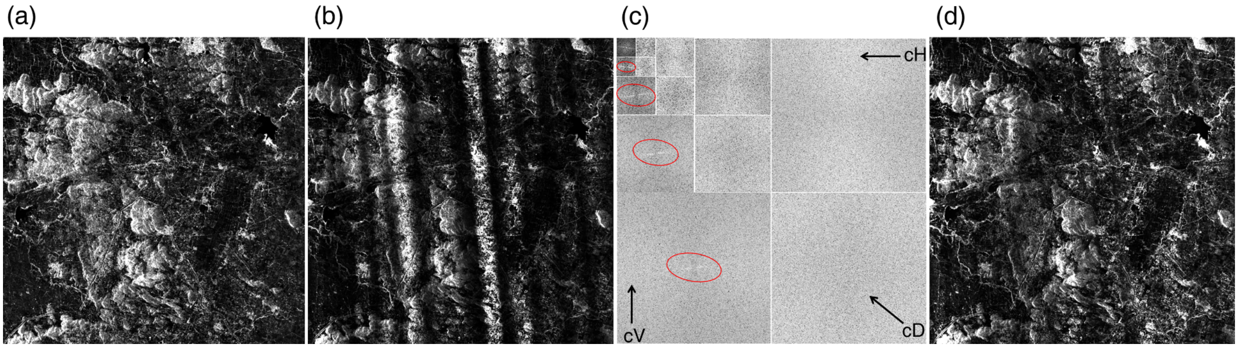

Fig. 5. Example of amplitude scintillation correction in POLSAR data [T] matrix element of T_{33} magnitude using the proposed approach. The area under correction is the subset in Scene 1 (Fig. 2). (a) Original reference data, (b) Original-disturbed data, (c) 2-D FFT power spectrum of the level 4, 2-D DWT coefficients and (d) Corrected data. High frequencies corresponding to the amplitude scintillation stripes in the power image are observed as bright features in the frequency domain (highlighted by the red ellipse). Signatures of the stripe artifacts are visible only in the vertical detailed coefficient (cV).

non-linear strategy of averaging-post-thresholding (Mohanty and Singh, 2019) is implemented for the FFT. Details of the popular Haar wavelet function, its use in multi-level DWT and the non-linear FFT filter used in our proposed methodology are elaborated below.

3.2.1. Haar function in multi-level DWT

We have applied a multi-level, 2-D DWT using the Haar wavelet function in the proposed mixed DWT-FFT approach for correction of POLSAR [T] matrix data affected by amplitude scintillation stripes. The Haar wavelet basis is obtained by a multiresolution of piecewise constant approximation (PCA) functions (Mallat, 1999). The highest DWT decomposition level/resolution for each [T] element is decided at which the stripes are no longer visible in the approximate and detailed coefficients. For all the POLSAR [T] matrices data, utilized in our study, the maximum level of DWT decomposition was fixed at level $i = 4$. Beyond this level, the image resolution became coarser making the identification of higher frequencies in the FFT power spectrum difficult.

Because of the lone vanishing moment of the Haar, the Haar Wavelet Transform (HWT) is generally not suited well for approximating smooth functions. Nonetheless, it is extremely efficient in analyzing signals with sudden transitions and in detecting sharp edges. This property of the HWT has been exploited in identifying the scintillation-induced stripes and filtering them using the FFT technique. Furthermore, the HWT is conceptually simple, memory efficient, computationally inexpensive, and exactly reversible. Compared to the FFT that has a computation time of $O(n \log n)$, where n is the number of pixels in an image, DWT-FFT with Haar wavelet has a $O(n)$ computation time (Münch et al., 2009).

3.2.2. Non-linear FFT (averaging-post-thresholding) strategy

Post DWT, the approximate and detailed coefficients at all levels are subjected to 2-D FFT. Depending upon the orientation of the stripes in the SAR image, the FFT spectra of the respective detailed coefficients showed bright pixels corresponding to high frequency components. To better visualize the isolated-linear bright features in the FFT spectrum, a transformation factor $0.07 \times \log(1 + abs(FFT))$ is applied. This transformation factor primarily assists in identifying the high frequency pixels to be corrected. The non-linear FFT strategy of averaging-post-thresholding applied on the spectrum is a two-step approach. The first step applies a threshold on the selected high frequency pixels. It is followed by replacing these selected pixels with an average of a 3×3 moving window. The efficacy of this filtering approach over traditional linear strategy (zero-masking) and other non-linear strategy (simple thresholding operation) has been discussed and illustrated with several examples in Mohanty and Singh (2019).

After the FFT filtering, inverse FFT (IFFT) is applied on the detailed DWT coefficients that were corrected. Following this, the sequential (level-wise) image reconstruction is performed using the combination of original- and corrected-DWT coefficients of that particular level, until the original image size is achieved. The $[T]_{amplitude}$ matrix, post correction, are combined with the $[T]_{phase}$ to retrieve back the corrected complex relative phase [T] matrix. The step-by-step processes explained in Section 3.1 and Section 3.2 are shown in the process flowchart of Fig. 3. Validation of the proposed methodology is made by comparing the POLSAR [T] matrix data measurements of reference data, original-disturbed data, and corrected results. The next section details the quantitative analysis of corrected data.

3.3. Post-processing of corrected [T] matrix

The subsection includes procedures from the different post-processing analyses that have been performed on the [T] matrix data corrected for amplitude scintillations stripe artifacts and compared with the corresponding $[T]_{reference}$ and $[T]_{disturbed}$ matrices. Supervised Wishart classification along with decomposition of [T] matrices into scattering powers using the 7SD model are performed on the data. Results of qualitative and quantitative analyses from the above mentioned processes are reported and the improvement due to correction of amplitude scintillation affected [T] matrix is thus demonstrated. Graphical representation of all the analyses implemented in this study is represented in Fig. 4.

3.3.1. Wishart supervised classification

Potential of the proposed mixed DWT-FFT approach in the correction of amplitude scintillation stripe in POLSAR [T] matrix is demonstrated. Apart from the qualitative analysis (shown in Section 4.1), we take the assessment further by performing a supervised Wishart classification (Lee and Grunes, 1994) on the reference-, disturbed-, and corrected- [T] matrices. The classifier maximizes the probability density function of the target pixels' [T] matrix, and is therefore statistically optimal (Lee et al., 1999). Results from the Wishart classification are explained in Section 4.2.

3.3.2. Comparison of scattering powers from 7SD model

Ever since the introduction of scattering power decomposition using physical scattering models for elements of [T] matrix, these models have been quite popular in the SAR fraternity as well as among the users of POLSAR data. Ease of implementation accompanied by accurate interpretation and classification of naturally-occurring targets have been the biggest advantages for the popularity of these models (Freeman and Durden, 1998; Yamaguchi et al., 2005). The latest addition to this list is the 7SD model (Singh et al., 2019). The model divides the average coherency matrix $\langle[T]\rangle$ into seven individual scattering power submatrices given as

$$[T] = P_s[T]_s + P_d[T]_d + \begin{cases} P_v[T]_{vol}^{dipole} \\ P_v[T]_{vol}^{dihedral} \end{cases} + P_h[T]_h + P_{od}[T]_{od} + P_{cd}[T]_{cd} + P_{md}[T]_{md} \tag{3}$$

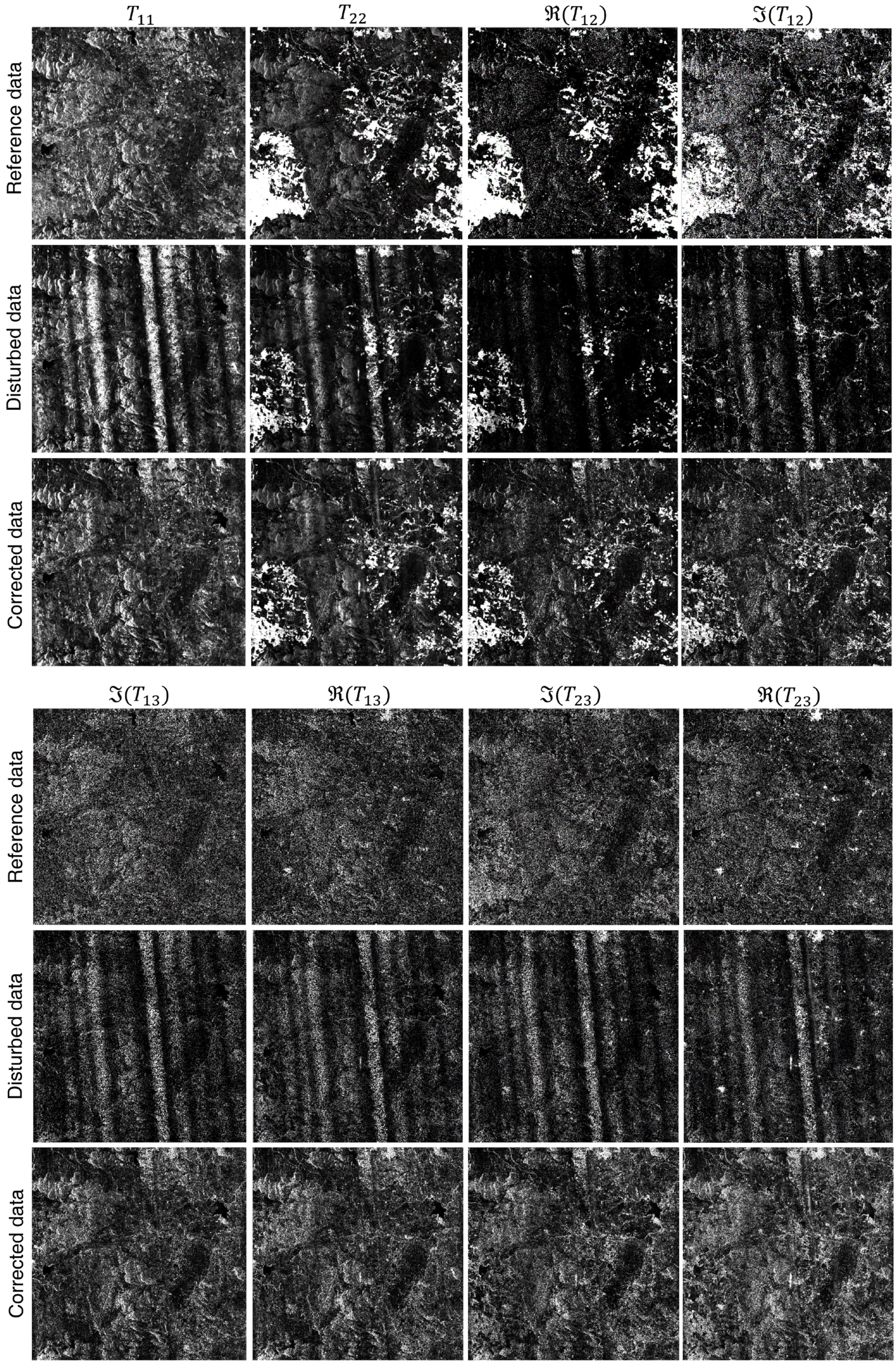

Fig. 6. [T] matrix elements for the subset in Scene 1 illustrating the refernce dataset, original-disturbed dataset, and corrected datasets.

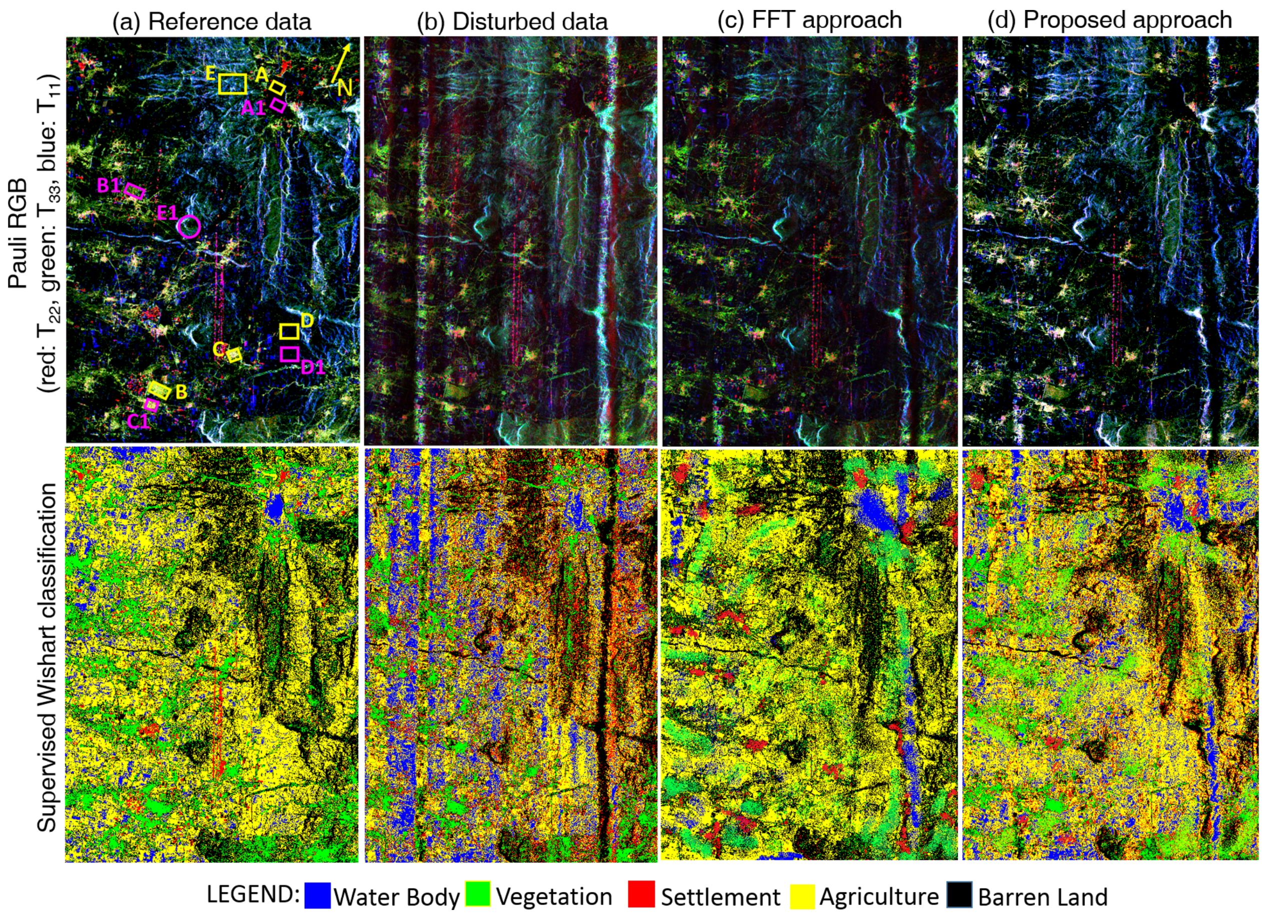

Fig. 7. Supervised Wishart classification results of [T] matrices for the subset in Scene 2 (Fig. 2). Top row: Pauli RGB representation of data (a) reference, (b) disturbed, (c) corrected using FFT approach, and (d) corrected using proposed approach. Bottom row: Classification results for the corresponding [T] matrices. Five classes (A-water body, B-vegetation, C-settlement, D-agriculture land, and E-barren land) used for the classification are highlighted in the reference day image. Training samples are highlighted in yellow boxes and the testing samples are illustrated by magenta boxes and class names suffixed by 1. (For interpretation of the references to colour in this figure legend, the reader is referred to the web version of this article.)

$$
\begin{aligned}
[T] &= \begin{bmatrix} T_{11} & T_{12} & T_{13} \\ T_{21} & T_{22} & T_{23} \\ T_{31} & T_{32} & T_{33} \end{bmatrix} \\
&= \frac{P_s}{1+|\beta|^2}\begin{bmatrix} 1 & \beta^* & 0 \\ \beta & |\beta|^2 & 0 \\ 0 & 0 & 0 \end{bmatrix} + \frac{P_d}{1+|\alpha|^2}\begin{bmatrix} |\alpha|^2 & \alpha & 0 \\ \alpha^* & 1 & 0 \\ 0 & 0 & 0 \end{bmatrix} \\
&+ P_v \left\{ \begin{array}{l} \frac{1}{30}\begin{bmatrix} 15 & -5 & 0 \\ -5 & 7 & 0 \\ 0 & 0 & 8 \end{bmatrix}, \text{cosine distribution} \\ \frac{1}{4}\begin{bmatrix} 2 & 0 & 0 \\ 0 & 1 & 0 \\ 0 & 0 & 1 \end{bmatrix}, \text{uniform distribution} \\ \frac{1}{30}\begin{bmatrix} 15 & 5 & 0 \\ 5 & 7 & 0 \\ 0 & 0 & 8 \end{bmatrix}, \text{sine distribution} \\ \frac{1}{15}\begin{bmatrix} 0 & 0 & 0 \\ 0 & 7 & 0 \\ 0 & 0 & 8 \end{bmatrix}, \text{oriented dihedral} \end{array} \right\} \\
&\frac{P_h}{2}\begin{bmatrix} 0 & 0 & 0 \\ 0 & 1 & \pm j \\ 0 & \mp j & -1 \end{bmatrix} + \frac{P_{od}}{2}\begin{bmatrix} 1 & 0 & \pm 1 \\ 0 & 0 & 0 \\ \pm 1 & 0 & 1 \end{bmatrix} \\
&+ \frac{P_{cd}}{2}\begin{bmatrix} 1 & 0 & \pm j \\ 0 & 0 & 0 \\ \mp j & 0 & 1 \end{bmatrix} + \frac{P_{md}}{2}\begin{bmatrix} 0 & 0 & 0 \\ 0 & 1 & \pm 1 \\ 0 & \pm 1 & 1 \end{bmatrix}
\end{aligned} \tag{4}
$$

Seven scattering powers P_s, P_d, P_v, P_h, P_{cd}, P_{od}, and P_{md} correspond to surface scattering, double-bounce scattering, volume scattering, helix scattering, compound dipole scattering (oriented quarter-wave reflector scattering), oriented dipole scattering, and mixed dipole scattering, respectively. Solution to the above equations and details about the expansion of the individual scattering submatrices, $\langle[T_s]\rangle$, $\langle[T_d]\rangle$, $\langle[T_{vol}]\rangle$, $\langle[T_h]\rangle$, $\langle[T_{cd}]\rangle$, $\langle[T_{od}]\rangle$ and $\langle[T_{md}]\rangle$, are given in Singh et al. (2019). 7SD is directly applied on $[T]_{reference}$, $[T]_{disturbed}$ and $[T]_{corrected}$. We then compare the scattering powers derived from $[T]_{corrected}$ with those obtained from $[T]_{reference}$ and $[T]_{disturbed}$ matrices for the individual datasets.

Table 2
Comparison of Wishart classification accuracies.

Data	$[T]_{reference}$	$[T]_{disturbed}$	$[T]^{FFT}_{corrected}$	$[T]^{DWT-FFT}_{corrected}$
Overall Accuracies (OA) (in %)	81.57	69.31	73.49	76.49
Kappa Coefficient ($\hat{k}$)	0.71	0.54	0.62	0.68

3.3.3. 2-D FFT based existing method and comparison with the proposed method

A 2-D FFT based amplitude scintillation correction approach is implemented on scattering power images derived from the 'four-component scattering power decomposition with an extended volume scattering model (S4R)' (Sato et al., 2012) based decomposition as demonstrated in Mohanty and Singh, 2019. The non-linear 2-D FFT technique (averaging-post-thresholding) demonstrated greater potential in correction of the amplitude scintillation stripes from scattering

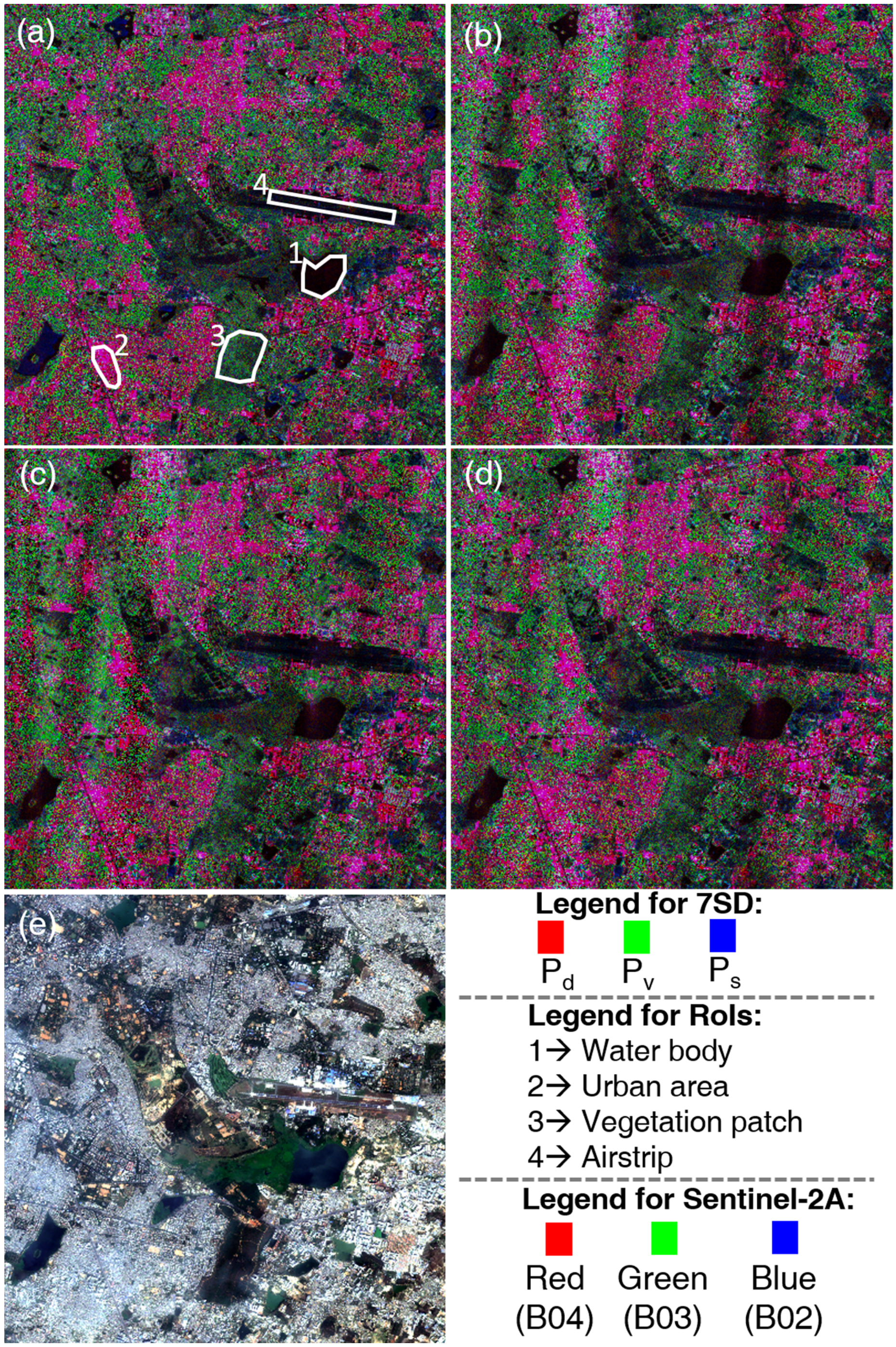

Fig. 8. 7SD RGB color composite (red = double-bounce scattering P_d, green = volume scattering P_v, and blue = surface scattering P_s) of datasets (a) reference, (b) disturbed, (c) corrected by the FFT approach, and (d) corrected by the proposed approach, over the city of Bengaluru, India, highlighted in subset of Scene 3 (Fig. 2). (e) Registered and resampled true color composite (red = Band 04, green = Band 03, and blue = Band 02) of the Sentinel-2A MSI optical image of the same area is also shown. Patches (RoIs) for which mean scattering power statistics is computed are highlighted by the white polygons in the reference data. (For interpretation of the references to colour in this figure legend, the reader is referred to the web version of this article.)

powers. Therefore, it has been adopted in the proposed method for comparative analysis. We have applied the existing method of 2-D FFT based approach (henceforth referred to as FFT approach) directly on the 7SD scattering power images derived from $[T]_{disturbed}$ matrix to correct them. Although 7SD scattering powers can be directly corrected using the correction technique, they restrict the effectiveness of POLSAR data for several other applications. Understanding the importance of [T] matrix, we have attempted to correct it for amplitude scintillation using the proposed approach and compared its performance with the FFT approach. Keeping this in mind, a comparative analysis is also performed between the scattering powers generated from the corrected [T] matrix using the proposed method, and the scattering powers corrected directly using the existing FFT approach. Results from this evaluation is reported in Section 4.3.

4. Results and discussion

After the amplitude scintillation stripe correction, results from the

Table 3
Representation of the mean scattering powers from 7SD model for the different patches (RoIs) selected in Scene 3 over city of Bengaluru, India. For each RoI, the statistics are reported for the reference, disturbed, and corrected (FFT approach and proposed (DWT-FFT) approach) datasets. The dominant scattering power for each RoI is highlighted in bold font.

Patch 1: Water body (Dominant scattering power: P_s)							
	P_s	P_v	P_d	P_h	P_{od}	P_{cd}	P_{md}
Reference	**68.33**	10.08	8.15	3.33	3.55	3.34	3.22
Disturbed	**54.19**	11.06	24.20	2.10	2.13	2.67	3.64
FFT approach	**60.03**	13.49	9.14	3.47	4.16	3.96	5.74
Proposed approach	**63.86**	12.89	11.01	2.50	2.62	2.42	4.69
Patch 2: Urban area (Dominant scattering power: P_d)							
	P_s	P_v	P_d	P_h	P_{od}	P_{cd}	P_{md}
Reference	11.35	11.12	**56.61**	3.11	3.91	3.78	10.12
Disturbed	19.56	21.22	**39.46**	2.42	3.93	2.13	11.26
FFT approach	19.76	12.08	**47.17**	3.11	4.65	2.86	10.36
Proposed approach	17.75	12.37	**53.84**	2.10	3.62	1.9	8.39
Patch 3: Vegetation (Dominant scattering power: P_v)							
	P_s	P_v	P_d	P_h	P_{od}	P_{cd}	P_{md}
Reference	17.89	**45.09**	14.64	4.79	6.21	6.31	5.04
Disturbed	22.29	**36.30**	16.90	5.57	6.41	7.09	5.43
FFT approach	21.31	**37.54**	16.15	5.38	6.61	6.93	6.07
Proposed approach	20.34	**39.99**	16.57	5.09	6.11	6.68	5.20
Patch 4: Airstripe (Dominant scattering power: P_s)							
	P_s	P_v	P_d	P_h	P_{od}	P_{cd}	P_{md}
Reference	**57.72**	11.48	23.60	1.65	2.16	1.91	1.47
Disturbed	**50.29**	15.59	29.02	1.18	1.34	1.31	1.25
FFT approach	**53.52**	13.53	27.74	1.29	1.49	1.27	1.13
Proposed approach	**55.34**	15.41	24.04	1.29	1.24	1.41	1.26

post-processing comparative analysis are presented in this section. Performance of the proposed method is analyzed by applying it on different POLSAR datasets. An example is presented to show the qualitative improvement in the corrected [T] matrix. The visual improvement is observed in the elements of [T] matrix after correction. A supervised Wishart classification is also applied on one dataset to check the efficacy of the correction method. Furthermore, 7SD model is implemented on the two corrected [T] matrices ($[T]^{FFT}_{corrected}$ and $[T]^{DWT-FFT}_{corrected}$) and original [T] matrices ($[T]_{refrence}$ and $[T]_{disturbed}$) for comparative analysis. The visual and qualitative improvement in 7SD scattering power results are also demonstrated after correction. Taking the study further, a quantitative analysis i.e., comparison of the mean scattering power, is also performed on 7SD scattering powers derived from four data types ($[T]_{refrence}$, $[T]_{disturbed}$, $[T]^{FFT}_{corrected}$, and $[T]^{DWT-FFT}_{corrected}$) already explained. Outcomes from each investigation are presented below.

4.1. Correction of scintillation stripes from POLSAR [T] matrix

The proposed approach is applied to the amplitude scintillation affected [T] matrix elements of POLSAR data. Subsets highlighted by yellow rectangles in the POLSAR scenes shown in Fig. 2 serve as inputs to the proposed algorithm.

To demonstrate the process, a multi-level DWT decomposition (level $i = 4$) using the Haar wavelet is applied to the magnitude of T_{33} ($|T_{33}|$) image for the subset of Scene 1 (1). The reference day $|T_{33}|$ image is shown in Fig. 5(a). As illustrated in Fig. 5(b), the amplitude scintillation stripes in the $|T_{33}|$ image of the disturbed data are not perfectly vertical or horizontal, but slightly oblique. Stripes, representing noises, in $|T_{33}|$ are observed as bright distinct features and are oriented by some angle in the FFT spectrum. From the FFT spectra of the DWT coefficients, plotted in Fig. 5(c), it is apparent that amplitude scintillation-induced stripe artifacts have significant contribution in the vertical detailed coefficients (cV) of the DWT. The bright signatures of the stripes are highlighted in the FFT spectrum of cV_i (i = 1, 2, 3, 4) by red ellipses. As the stripes in the T_{33} image are oblique (away from the vertical axis), the same tilt (away from the horizontal axis) is observed in the corresponding FFT spectra also. The non-linear correction strategy, that works on the principle of pixel averaging after applying a threshold value, is applied on the cV spectra followed by an IFFT. Level-wise image reconstruction is further performed using the unaltered DWT coefficients $(cA, cH$, and $cD)_i$ and the corrected cV_is. Output from the correction of T_{33} is shown in Fig. 5(d).

For the same subset of Scene 1, correction results for the magnitude of remaining eight [T] elements (T_{11}, T_{22}, $|\Re(T_{12})|$, $|\Im(T_{12})|$, $|\Re(T_{13})|$, $|\Im(T_{13})|$, $|\Re(T_{23})|$, and $|\Im(T_{23})|$) are shown in Fig. 6, along with the reference data and original-disturbed data, thereby confirming the correction of each [T] element.

The proposed mixed DWT-FFT approach shows a definite visual improvement in the [T] matrix elements as demonstrated in Fig. 5 and Fig. 6. Besides correcting the striping effect due to amplitude scintillation, the approach is also successful in retaining target information from the original to the output image. This is further confirmed from the results of a supervised Wishart classification performed on the subset selected for Scene 2.

4.2. Performance evaluation of proposed method using supervised Wishart classification

In addition to demonstrating the potential of the proposed method in qualitative improvement of POLSAR [T] matrix data, we take the assessment further by performing a supervised Wishart classification on $[T]_{reference}$, $[T]_{disturbed}$, and $[T]_{corrected}$ matrices from the existing FFT method and the proposed approach ($[T]^{FFT}_{corrected}$ and $[T]^{DWT-FFT}_{corrected}$) for the subset of Scene 2. Five classes chosen for classification are water body, agricultural land, small settlement areas, vegetation patches and barren land. The regions of interest (RoIs) for training and testing pixels are highlighted by yellow and magenta polygons respectively, in the Pauli RGB image of the reference dataset (Fig. 7(a) top row). The corresponding supervised Wishart classification results for reference-, disturbed-, and corrected- data are shown in Fig. 7 (bottom row). The quantitative analysis for the classification is reported in Table 2.

The reported overall accuracy (OA) and kappa coefficient ($\hat{k}$) are highest for the reference day data and lowest for the disturbed day. Values from the proposed correction method (OA = 76.49%, $\hat{k} = 0.68$) as well as the existing FFT approach (OA = 73.49%, $\hat{k} = 0.62$) are greatly improved over the disturbed data (OA = 69.31%, $\hat{k} = 0.54$). However, the proposed method performs fairly better than the FFT approach with classification accuracies closely comparable to the reference data (OA = 81.57%, $\hat{k} = 0.71$). These improved results further validate the applicability of the proposed approach to several POLSAR measurements and various applications of the [T] matrix acquired during amplitude scintillation conditions.

4.3. Comparative analysis of amplitude scintillation stripe correction in scattering power images

Correction of the [T] matrix elements using the proposed approach gives freedom to the appropriateness and applicability of the POLSAR data in a way that it can be utilized for other applications. Taking this into account, we have, divided the $[T]^{DWT-FFT}_{corrected}$ into seven scattering power submatrices using the 7SD model. The scattering powers derived from the $[T]_{reference}$, $[T]_{disturbed}$, and $[T]^{DWT-FFT}_{corrected}$ are compared with the scattering powers directly corrected using the FFT approach. This section is divided into two parts. In the first analysis, the subset chosen in Scene 3 over the city of Bengaluru, India, is thoroughly analyzed in terms of scattering powers from several targets. In the second part, comparison of the mean scattering powers over individual RoIs of Scene 1, 2, 4, 5 and 6 is performed and the results are reported. Furthermore, the individual dominant scattering power value (P_s, P_d and P_v) images are also provided in Figs. S1 to S6 (see supplementary file) for scene 1 to scene 6, respectively.

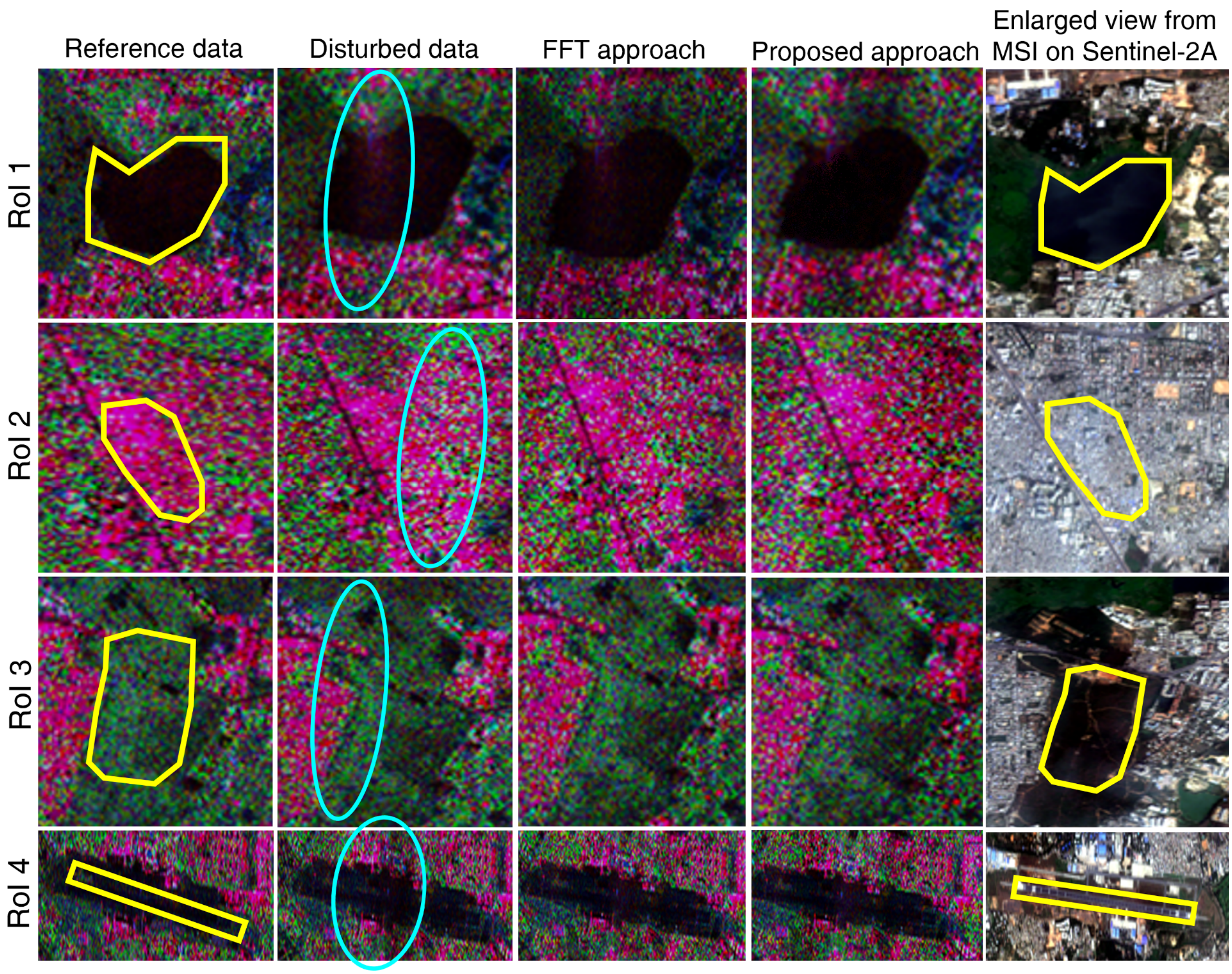

Fig. 9. Enlarged views of the RoIs shown in Fig. 8 highlighted by yellow polygons. The corresponding optical image from MSI onboard Sentinel-2A is also enlarged to represent that the RoIs are permanent land-cover features. RoIs affected by the amplitude scintillation stripes are encircled by cyan colored ellipse. (For interpretation of the references to colour in this figure legend, the reader is referred to the web version of this article.)

4.3.1. Scene 3: Bengaluru city, India

Fig. 8 shows the qualitative comparison between the RGB color coded 7SD scattering power images (red: double-bounce scattering P_d, green: volume scattering P_v, and blue: surface scattering P_s) of the subset in Scene 3. This region lies within Bengaluru, India and comprises of several natural and manmade targets. 7SD scattering powers obtained after decomposition of $[T]^{DWT-FFT}_{corrected}$, $[T]_{reference}$, $[T]_{disturbed}$ datasets and corrected results from the FFT approach are shown in Fig. 8. In addition to the visual analysis, a quantitative validation of the proposed approach is assessed by comparing the dominant 7SD-derived mean scattering power for each target.

Four patches are selected over which the mean scattering powers are compared and contrasted to demonstrate the effectiveness and reliability of our proposed method in the correction of amplitude scintillation stripes. These patches (RoIs) are chosen over targets such as (1): water body, (2): urban area, (3): vegetation patch, and (4) airstrip. They are strategically chosen so as to include targets that are visible and permanent, i.e., they would not have changed over the period of second data acquisition. To validate that the RoIs taken are permanent land features, a true color composite (red: Band 04, green: Band 03, and blue: Band 02) of the optical image acquired by the multispectral instrument (MSI) on board Sentinel-2A is also included in Fig. 8. Since the optical image is used to identify the targets under observation, we have registered the Sentinel-2A MSI data with the PALSAR-2 image and resampled it to the resolution of the SAR data (~45 m ground resolution after multilooking). These RoIs are highlighted by the white polygons in the 7SD RGB color composite of the reference data. The corrected data is a result of implementing the proposed approach and the FFT approach (previously explained in Mohanty and Singh (2019)). Results from the FFT approach are included to highlight improvements in corrected results using the proposed mixed DWT-FFT method. The dominant scattering power corresponding to each RoI is identified and the analysis of its improvement in the corrected data is described in Table 3. Although Fig. 8 demonstrates results from the correction approaches for the larger subset, we have also provided enlarged views of the RoIs under consideration for improved visualization purpose. They are shown in Fig. 9. Along with the RoI, marked by the yellow polygon, we have also highlighted the presence of amplitude scintillation stripe signature(s) (cyan colored ellipse) that are corrected in the figure.

Patch 1 (water body) taken over the Bellandur lake demonstrates dominant surface scattering power P_s. Due to the amplitude scintillation stripes, the P_s power is reduced from 68.3% to 54.2%. After correction using the proposed approach, it improves to 63.86% from a value of 60.03% obtained after correction from the existing FFT approach. While there is a 9.6% improvement over the disturbed day statistics, using the proposed approach, the improvement over the FFT technique is also good, i.e., 3.8%. Similarly, for the patch 2 over the urban area, double-bounce scattering power P_d is the highest in all data types. However, the increase from 39.46% in the disturbed data, to 53.84% in corrected data from the proposed approach demonstrates the performance of the mixed DWT-FFT correction strategy. The P_d statistics over patch 2 in the reference data is 56.61% and lower P_d value of 47.17% is

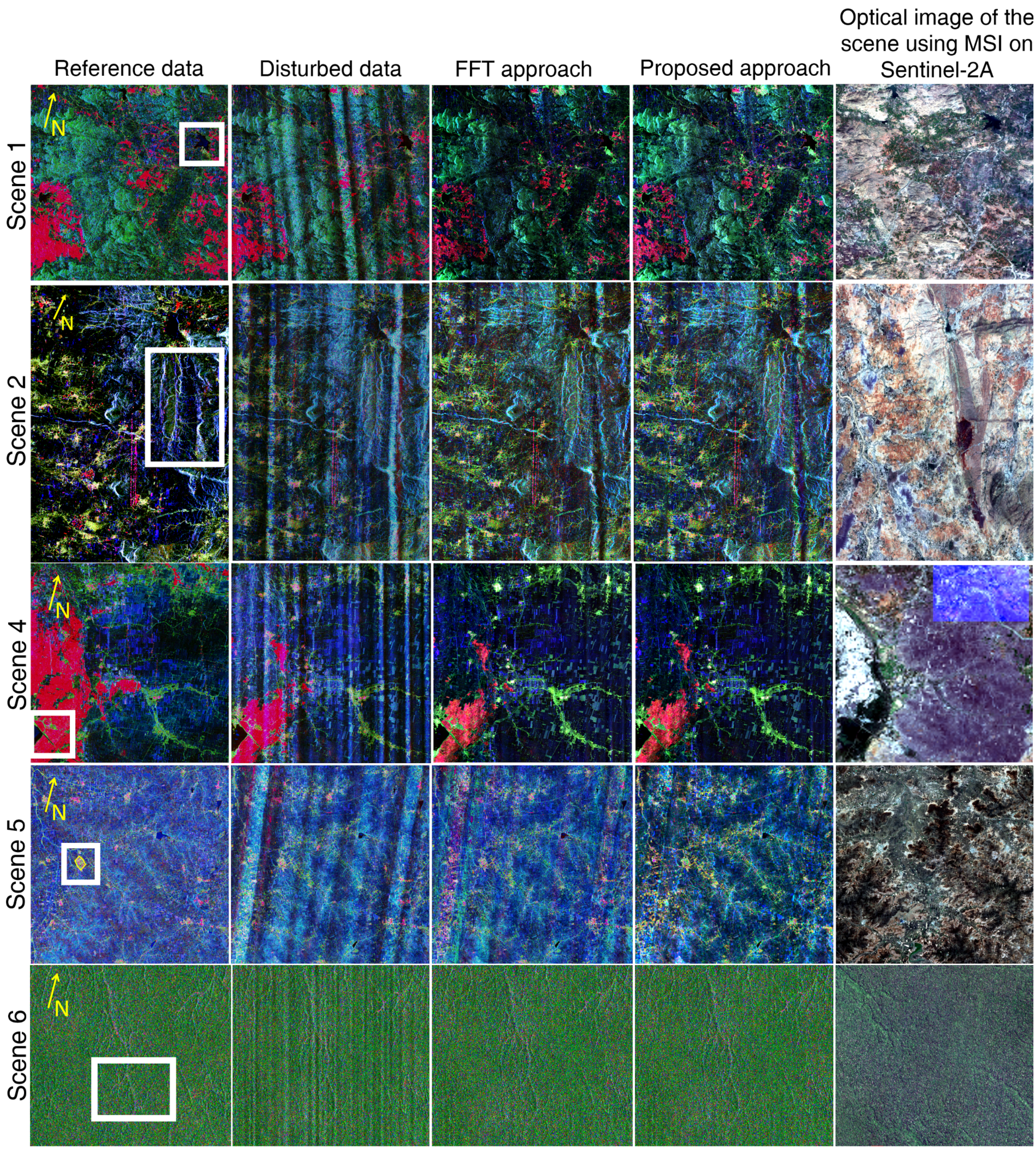

Fig. 10. 7SD RGB color composites (red = double-bounce scattering, green = volume scattering, and blue = surface scattering) of ALOS-2/PALSAR-2 and ALOS/PALSAR datasets demonstrating the qualitative comparison of the proposed mixed DWT-FFT approach alongside the reference-, disturbed-, and FFT approach corrected datasets. The regions shown here are subsets of the scenes detailed in Fig. 2. The left panel shows the 7SD color composite images of the references days under non-scintillation conditions, followed by the disturbed day data and results from the amplitude scintillation correction algorithms of 2-D FFT approach and the proposed DWT-FFT method. The right-most panel shows the corresponding areas in true color composite (red = Band 04, green = Band 03, and blue = Band 02) of Sentinel-2A MSI optical image. White rectangles in the reference data indicate area of the RoIs selected for quantitative analysis. Enlarged views of the same are shown in Fig. 11. (For interpretation of the references to colour in this figure legend, the reader is referred to the web version of this article.)

achieved by the FFT approach. Among the compound scattering powers, contributions of P_{md} is comparable to P_s and P_v powers. This is because of the mixed dipole type scattering coming from urban structures (Singh et al., 2019). .

For the patch 3 selected over a vegetation patch has contributions from P_s, P_d and P_v scattering powers. However, P_v is the dominant power as observed by the 45% contribution of P_v in the reference data. Compared to the disturbed data, P_v power is improved from 36.3% to 37.54% in the FFT approach and 40% in the proposed approach. For the final target type, patch 4 is chosen over the airstrip (Hindustan Aeronautics Limited), where P_s is the dominant scattering power. Implementing the proposed approach, P_s power is improved from 50.29% (disturbed) to 55.34% (DWT-FFT corrected) compared to 57.72% (reference). Although the P_s power from the FFT approach (53.52%) is better than the disturbed day's statistics, the performance of the proposed method is still better. Comparison of mean scattering

Table 4

Representation of the mean scattering powers from 7SD model for the different patches (RoIs) selected in scenes 1, 2, 4, 5 and 6. For each RoI, the statistics are reported for the reference, disturbed, and corrected (FFT approach and proposed (DWT-FFT) approach) datasets. The dominant scattering power for each RoI is highlighted in bold font.

	P_s	P_v	P_d	P_h	P_{od}	P_{cd}	P_{md}
Scene 1: Water body (Dominant scattering power: P_s)							
Reference	**81.07**	6.87	8.24	0.68	0.66	1.23	1.23
Disturbed	**72.82**	11.37	10.61	1.27	1.12	1.11	1.67
FFT approach	**74.86**	10.75	9.79	1.45	0.82	0.95	1.37
Proposed approach	**77.09**	9.65	9.37	1.15	0.77	0.89	1.06
Scene 2: Barren land (Dominant scattering power: P_s)							
	P_s	P_v	P_d	P_h	P_{od}	P_{cd}	P_{md}
Reference	**66.23**	9.79	15.12	3.34	2.06	1.82	1.64
Disturbed	**55.04**	13.48	20.79	3.49	2.64	2.27	2.27
FFT approach	**59.62**	10.71	17.62	3.25	3.43	2.19	3.18
Proposed approach	**62.83**	8.25	16.50	3.24	2.99	3.12	3.07
Scene 4: Water body (Dominant scattering power: P_s)							
	P_s	P_v	P_d	P_h	P_{od}	P_{cd}	P_{md}
Reference	**80.71**	6.79	7.12	1.34	1.56	1.04	1.43
Disturbed	**73.04**	10.18	10.79	1.49	1.64	1.27	1.57
FFT approach	**75.62**	9.67	9.76	1.25	1.41	1.11	1.18
Proposed approach	**77.76**	8.28	8.47	1.24	1.49	1.18	1.57
Scene 5: Settlement area (Dominant scattering power: P_d)							
	P_s	P_v	P_d	P_h	P_{od}	P_{cd}	P_{md}
Reference	21.49	23.29	**39.15**	2.6	3.41	5.5	4.64
Disturbed	24.94	30.96	**26.12**	2.6	3.15	4.3	7.9
FFT approach	24.18	28.57	**32.28**	2.3	2.45	3.35	6.8
Proposed approach	24.52	26.66	**34.65**	1.86	2.28	3.63	6.4
Scene 6: Forest (Dominant scattering power: P_v)							
	P_s	P_v	P_d	P_h	P_{od}	P_{cd}	P_{md}
Reference	18.96	**48.88**	10.89	4.59	6.11	5.93	4.64
Disturbed	21.64	**42.37**	11.63	5.36	6.66	7.02	5.32
FFT approach	20.83	**44.19**	11.01	5.21	7.02	6.78	4.95
Proposed approach	18.83	**47.53**	10.36	4.99	6.59	6.67	5.03

power statistics of these patches indicate that the proposed approach corrects the amplitude scintillation affected POLSAR datasets better than the existing 2-D FFT method.

4.3.2. Other datasets (Scenes 1, 2, 4, 5, and 6)

Additional examples of visual improvement in scattering powers using the proposed approach are shown in Fig. 10. Similar to the Scene 3, RoIs are chosen in these individual scenes and their scattering power statistics are reported in Table 4. Furthermore, enlarged views of the RoIs along with the optical data from MSI on board Sentinel-2A are shown in Fig. 11. The optical image aids in identifying and confirming that RoIs selected are permanent features and visible in the data.

In Fig. 11, acquired by ALOS-2/PALSAR-2 over south-central India, the region highlighted in Scene 1 lies to the south of river Krishna, near the town of Devadurga in Karnataka. The terrain is dotted with several land features such as scattered urban settlements, water bodies, small shrub-like vegetation, patches of agricultural land, etc. For the quantitative analysis, a small water body is identified as the RoI in the scene (highlighted by the white polygon in the reference data of Fig. 10 (first row)). This inland water body is a permanent feature that has not changed over the time period of the two acquisitions and has relatively smooth surface compared to the low frequency radar signals. In this RoI, surface scattering P_s is expected to be the dominant scattering mechanism. And, as expected, we observe the highest contribution by P_s (81.07% in reference data) as shown in Table 4 (first row). However, a 8.25% decrease in P_s is seen during the disturbed condition (P_s = 72.82%) of amplitude scintillation. After corrections, this value is improved in both FFT approach and the proposed approach to 74.86% (~2%) and 77.09% (~4.5%), respectively. Nevertheless, efficacy of the proposed method over the FFT approach is clearly exhibited from the visual improvement. Apart from the three main scattering powers: P_s, P_d, and P_v, others have almost negligible contribution (~<1.5%). This is because, the scattering powers (P_h, P_{cd}, P_{od}, and P_{md}) are better suited to targets demonstrating compound scattering behaviour, such as urban built-up areas, targets oriented at an angle to the radar's line of sight, as well as in vegetations.

In another example, the RoI chosen in Scene 2 (Fig. 10: second row) is a bare ground near the Pavagada solar park at the borders of the southern states of Andhra Pradesh and Karnataka in India. The land is undulating and marred with sparse vegetation. At some distance, within the RoI, are windmills installed by the state government. The statistics of the mean scattering powers from 7SD calculated over the RoI are presented in Table 4 (second row). As indicated, the surface scattering power P_s is the dominant scattering for targets such as barren land, open fields, flat plains, etc. In addition to P_s, contributions from double-bounce scattering P_d coming from the erected windmills and volume scattering from the sparse vegetation are small and cannot be ignored. However, we are interested in comparing the dominant scattering power P_s only. A ~11% decrease in the dominant P_s power is observed in the disturbed data statistics (55.04%) compared to the reference data 66.23%. Implementing the correction approaches of FFT and the proposed method, improvement in P_s power is reported. While the P_s is 59.62% from the FFT approach (improvement of 4.6%), it is further increased to 62.83% using the proposed method (improvement of 7.8%). The corrections also reduce the high values of P_d and P_v in the disturbed data to values that are comparable with the statistics of the reference data. The contributions from compound scattering powers are minor and hence, are not taken into consideration.

Similar to Scene 1, the RoI chosen in Scene 4 (Fig. 10: third row) for comparative analysis of mean scattering powers is also taken over a permanent water body. In this case, the Kanekal water tank located south of Bellary city is used as the RoI. Dominant surface scattering P_s = 80.71% is observed for the reference data as the inland water body acts a specular reflector. The decrease in P_s from 80.71% to 73.04% (7.7%) in the disturbed day statistics is improved to 75.62% and 77.76% by implementing the FFT approach and the proposed approach, respectively. These statistics are reported in Table 4. We have not considered the minor contributions from other scattering powers.

Furthermore, the small town of Gulbarga, in the state of Karnataka, is the landmark of the ALOS-2/PALSAR-2 Scene 5 (Fig. 10: fourth row) under investigation. Small subset of the region chosen for stripe correction consists of small rural settlements, farming lands, and spare vegetation cover. For the statistical analysis of the scattering powers, we have chosen a small built-up area (village) named Nimbarga. As previously mentioned, this RoI is a permanent feature and comprises of few houses, sparse vegetation in the form of trees and shrubs, and road networks. The quantitative analysis of this heterogeneous RoI, shown in Table 4 (fourth row), highlights some interesting results. All seven scattering powers have significant contribution in the statistics. Since, the RoI is chosen over a sparsely populated village, the double-bounce power P_d is the largest (39.15%), followed by equal contributions from P_s, and P_v. Hence, we will be concentrating on these three scattering powers only for the comparison. The P_d power increased from 26.12% (for disturbed data) to 34.65% (~8%) using the proposed correction approach. Even the P_v is reduced by 4.3% using this technique. However, for FFT approach the scattering power improvements are lower than the proposed approach. This example also highlights the adeptness of the correction method in removing image artifacts produced by even ionospheric amplitude scintillations. The surface scattering power P_s is almost the same from corrections using FFT approach and the proposed method.

A small area from Scene 6 (Fig. 10: last row) of ALOS/PALSAR over the Amazon forest was also selected and the proposed method was applied. This RoI consists of dense evergreen trees that form a very thick canopy preventing even long wavelength L-band SAR signal from penetrating. Thus, most of the scattering comes from the canopy imparting a dominant volume scattering P_v component to the scene. This is

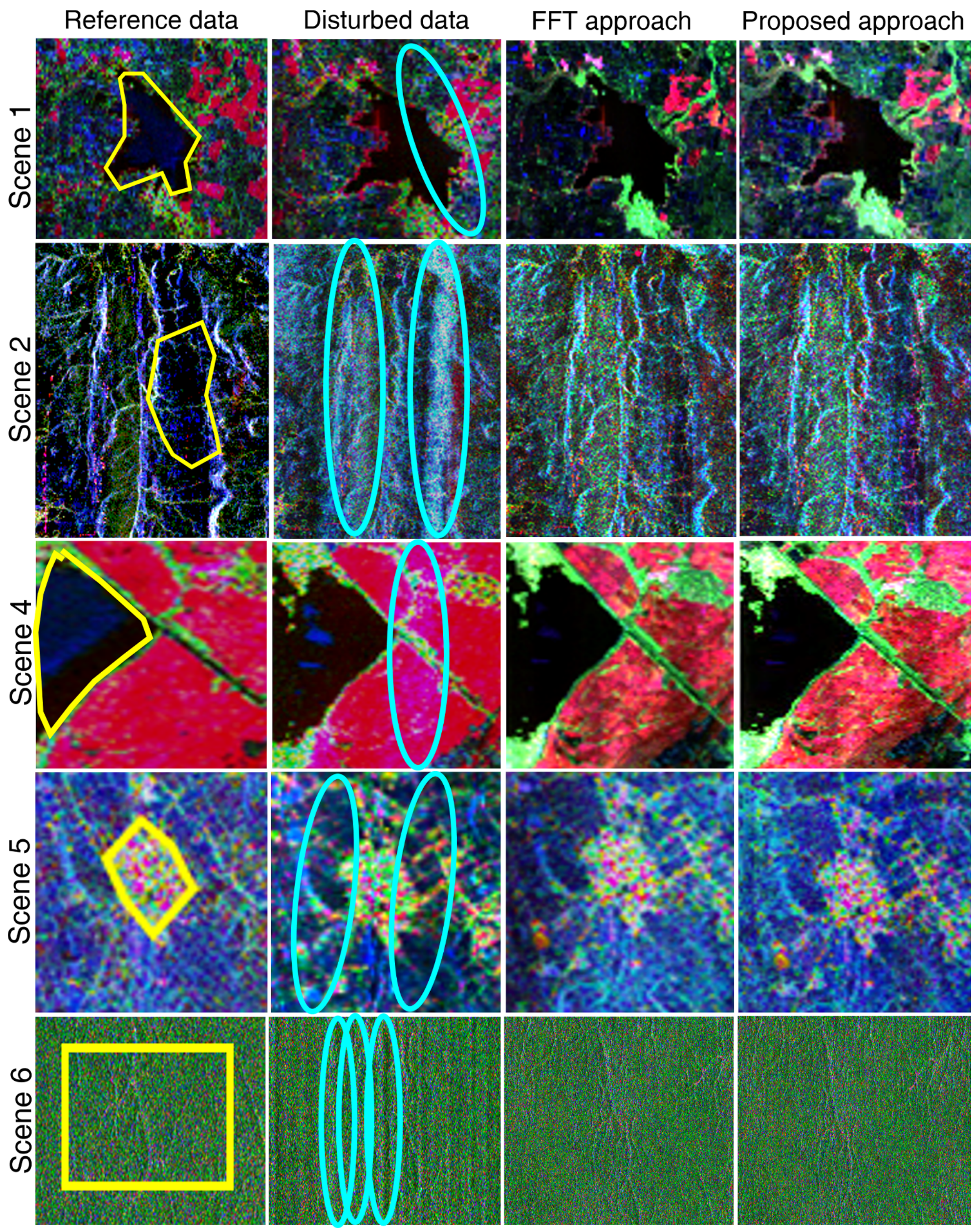

Fig. 11. Enlarged views of the areas marked by the white rectangles in Fig. 10. The RoIs are highlighted by yellow polygons in the reference day image. Regions of the RoIs affected by amplitude scintillation stripes are encircled by cyan colored ellipse. (For interpretation of the references to colour in this figure legend, the reader is referred to the web version of this article.)

observable in the primarily green tone of the RGB composite of the scattering power decomposition image (Fig. 10, last row). As demonstrated in Table 4 (last row), the dominant power $P_v = 48.88\%$ is reduced by 6.5% in the disturbed data under the condition of severe amplitude scintillations. Upon correction, the proposed technique $P_v = 47.53\%$ shows an improvement of 5.1%, while the FFT approach $P_v = 44.19\%$ shows a mere 1.8% increase compared to the disturbed data $P_v = 42.37\%$. Minor decrease in other scattering powers are also observed in the proposed correction method.

In scenes 4 and 6 the stripes are relatively vertical, and hence their removal is quite straightforward in both the proposed method and the FFT approach. However, some remains of the amplitude scintillation stripes are still observed in the post-correction results of the FFT approach for scenes 1, 2, 3 and 5. This occurs due to the difficulty in stripe identification in less-dominant scattering powers, incorrect identification of high frequency pixels in the Fourier spectrum, and highlights the inadequacy of the FFT approach. Outputs from the proposed method, however, do not show such strong remains since it is able to separate contributions from high- and low-frequency components better.

5. Conclusions

In the paper, we corrected amplitude scintillation-induced stripes in POLSAR [T] matrix data using an image correction and restoration approach. The proposed technique encompasses amplitude and relative phase component decomposition and uses a combination of multi-level DWT using the Haar wavelet function followed by the application of a non-linear FFT strategy. We have tested the operability and potential of this proposed technique on several POLSAR [T] matrix data that are affected by varied degree of amplitude scintillation stripes. These data are acquired by low frequency L-band SAR sensors, PALSAR and PALSAR-2, flown on-board Earth observation satellites ALOS and ALOS-

2, respectively. Data acquired under scintillation condition affect [T] elements and scattering powers in addition to target identification, image classification and accurate geophysical parameter retrieval. Efficacy of the proposed correction approach is qualitatively shown using visual analysis; the accuracy is quantified using Wishart classifier and the 7SD decomposition model. Application of the supervised Wishart classifier on the [T] matrices improved the overall accuracy and kappa coefficienta from 69.31% and 0.54 (for $[T]_{disturbed}$) to 76.49% and 0.68 (for $[T]_{corrected}^{DWT-FFT}$)). The statistics after correction are quite comparable to the $[T]_{reference}$ values of 81.57% and 0.71, respectively. Correction of the amplitude scintillation-induced stripes, using the proposed technique, is also tested by comparing the mean scattering powers, derived from 7SD model, with the existing 2-D FFT approach. Improvement in the dominant mean scattering powers are reported to be as high as 9.6% for certain target types, like waterbodies and barren land. For regions of interest composed of mixed targets, the dominant mean scattering powers are also improved (average 4.5%) from the disturbed day statistics. Although the FFT approach demonstrates correction of stripes and increase in scattering powers, results from the proposed mixed DWT-FFT correction techniques are always improved over those of the former. The proposed technique corrects the amplitude scintillation-induced stripes to a good extent along with preserving of background information.

Drawbacks of the proposed approach may constitute the inappropriate selection of the wavelet function. Wrong choice of the scaling and/or the wavelet functions may result in inaccuracies. Also, erroneous choice on the level of wavelet decomposition may introduce errors. This is because when DWT levels are decimated, the frequency resolution becomes coarser at each subsequent level. As a result, choosing the exact frequency corresponding to the stripe artifact is incorrect. This error is further translated in the output during reconstruction where either some stripes still persist or background information is removed at few pixels during filtering. The same rationale is also applied while determining the correct FFT strategy.

Despite several limitations in the individual DWT and FFT techniques, the proposed method, based on decomposition of amplitude and phase components and combining DWT-FFT transforms for removal of amplitude scintillation stripe correction performs effectively to improve the POLSAR [T] matrix data. The proposed method also highlights the improvement achieved in scattering powers derived from the corrected [T] matrix, an index for ascertaining the usability of the POLSAR data for further applications. In the current scenario, there are no physical models to correct for the amplitude scintillation-induced striping effects owing to the complexity of the ionosphere together with its interaction with SAR signal. Hence, the proposed method (accompanied by future modifications in the correction algorithm) can definitely serve as a potential tool in correcting amplitude scintillation affected POLSAR data acquired from low-frequency sensor data. Such techniques can be applied to currently operating satellites like ALOS-2/PALSAR-2 and those planned to be launched in the future such as P-band BIOMASS (Rogers et al., 2014) and NISAR (Pi, 2015) which is designed to operate at L- and S-band.

Declaration of Competing Interest

The authors declare that they have no known competing financial interests or personal relationships that could have appeared to influence the work reported in this paper.

Acknowledgment

The authors express their gratitude to JAXA for the ALOS/PALSAR and ALOS-2/PALSAR-2 data procured under RA6 Project No. 3169. The work is supported by the Department of Science and Technology, Government of India, under Grant DST/CCP/NHC/155/2018 (G). The authors also acknowledge the insightful discussions with Prof. V. M. Gadre, Department of Electrical Engineering, IIT Bombay, that helped in improving the manuscript. We also thank the anonymous reviewers for their careful reading of our manuscript and their insightful comments and suggestions.

Appendix A. Supplementary data

Supplementary data associated with this article can be found, in the online version, at https://doi.org/10.1016/j.isprsjprs.2020.04.005.

References

Belcher, D.P., Cannon, P., 2014. Amplitude scintillation effects on sar. IET Radar, Sonar Navigation 8, 658–666. https://doi.org/10.1049/iet-rsn.2013.0168.
Belcher, D.P., Rogers, N., 2009. Theory and simulation of ionospheric effects on synthetic aperture radar. IET Radar, Sonar Navigation 3, 541–551. https://doi.org/10.1049/iet-rsn.2008.0205.
Bickel, S.H., Bates, R.H.T., 1965. Effects of magneto-ionic propagation on the polarization scattering matrix. Proc. IEEE 53, 1089–1091. https://doi.org/10.1109/PROC.1965.4097.
Carfantan, H., Idier, J., 2010. Statistical linear destriping of satellite-based pushbroom-type images. IEEE Trans. Geosci. Remote Sens 48, 1860–14871. https://doi.org/10.1109/TGRS.2009.2033587.
Carrano, C.S., Groves, K.M., Caton, R.G., 2012. Simulating the impacts of ionospheric scintillation on l band sar image formation. Radio Sci. 47, 1–14. https://doi.org/10.1029/2011RS004956.
Chandrasekhar, E., Dimri, V.P., Gujijala, V.G., 2013. Geomagnetic jerks: A study using complex wavelets. In: Chandrasekhar, E., Dimri, V.P., Gadre, V.M. (Eds.), Wavelets and Fractals in Earth System Sciences. Taylor and Francis, CRC Press, Boca Raton, FL, pp. 195–218.
Chang, Y., Yan, L., Wu, T., Zhong, S., 2016. Remote sensing image stripe noise removal: From image decomposition. IEEE Trans. Geosci. Remote Sens. 54, 7018–7031. https://doi.org/10.1109/TGRS.2016.2594080.
Chen, J., Lin, H., Shao, Y., Yang, L., 2006. Oblique striping removal in remote sensing imagery based on wavelet transform. Int. J. Remote Sens. 27, 1717–1723. https://doi.org/10.1080/01431160500185516.
Chen, J., Shao, Y., Guo, H., Wang, W., Zhu, B., 2003. Destriping cmodis data by power filtering. IEEE Trans. Geosci. Remote Sens. 41, 2119–2124. https://doi.org/10.1109/TGRS.2003.817206.
Chen, Y., Huang, T., Zhao, X., Deng, L., Huang, J., 2017. Stripe noise removal of remote sensing images by total variation regularization and group sparsity constraint. Remote Sens. 9, 559. https://doi.org/10.3390/rs9060559.
Daubechies, I., 1990. Wavelet transform, time-frequency localization and signal analysis. IEEE Trans. Information Theory 36, 961–1005. https://doi.org/10.1109/18.57199.
Deergha Rao, K., Swamy, M.N.S., Plotkin, E.I., 2001. Image restoration using a hybrid approach based on DWT and SMKF. In: Proceedings 2001 International Conference on Image Processing (Cat. No.01CH37205), IEEE. https://doi.org/10.1109/ICIP.2001.959000.
Freeman, A., 2004. Calibration of linearly polarized polarimetric sar data subject to faraday rotation. IEEE Trans. Geosci. Remote Sens. 42, 1617–1624. https://doi.org/10.1109/TGRS.2004.830161.
Freeman, A., Durden, S.L., 1998. A three-component scattering model for polarimetric sar data. IEEE Trans. Geosci. Remote Sens. 36, 963–973. https://doi.org/10.1109/36.673687.
Fung, A.K., Chen, K.S., 2010. Microwave Scattering and Emission Models for Users. Artech House.
Gadallah, F.L., Csillag, G., Smith, E.M., 2000. Destriping multisensor imagery with moment matching. Int. J. Remote Sens. 21, 2505–2511. https://doi.org/10.1080/01431160050030592.
Horn, B.K.P., Woodham, R.J., 1979. Destriping landsat mss images by histogram modification. Comput. Graphics Image Process. 10, 69–83. https://doi.org/10.1080/01431160050030592.
Jiang, W., Yu, A., Dong, Z., Wang, Q., 2016. Comparison and analysis of geometric correction models of spaceborne SAR. Sensors 16, 1187–1202. https://doi.org/10.3390/s16070973.
Karim, S.A.A., Kamarudin, M.H., Karim, B.A., Hasan, M.K., Sulaiman, J., 2011. Wavelet transform and fast fourier transform for signal compression: A comparative study. In: 2011 International Conference on Electronic Devices, Systems and Applications (ICEDSA), IEEE. https://doi.org/10.1109/ICEDSA.2011.5959031.
Lee, J.S., Grunes, M.R., 1994. Classification of multi-look polarimetric sar imagery based on complex wishart distribution. Int. J. Remote Sens. 15, 2299–2311. https://doi.org/10.1080/01431169408954244.
Lee, J.S., Grunes, M.R., Ainsworth, T.L., Du, L.J., Schuler, D.L., Cloude, S.R., 1999. Unsupervised classification using polarimetric decomposition and the complex wishart classifier. IEEE Trans. Geosci. Remote Sens. 37, 2249–2258. https://doi.org/10.1109/36.789621.
Lee, J.S., Grunes, M.R., Pottier, E., 2001. Quantitative comparison of classification capability: fully polarimetric versus dual and single-polarization SAR. IEEE Trans. Geosci. Remote Sens. 39, 2343–2351. https://doi.org/10.1109/36.964970.
Lee, J.S., Pottier, E., 2009. Polarimetric Radar Imaging: From Basics to Applications. CRS Press.

Lee, M.C., Das Gupta, A., Klobuchar, J.A., Basu, S., Basu, S., 1982. Depolarization of vhf geostationary satellite signals near the equatorial anomaly crests. Radio Sci. 17, 399–409. https://doi.org/10.1029/RS017i002p00399.

Liu, J.G., 2006. Fft selective and adaptive filtering for removal of systematic noise in etm + imagedesy images. IEEE Trans. Geosci. Remote Sens. 44, 3716–3724. https://doi.org/10.1109/tgrs.2006.881752.

Mallat, S., 1999. A Wavelet Tour of Signal Processing. Academic Press.

Meher, S.K., Shankar, B.U., Ghosh, A., 2010. Multispectral remote sensing image classification using wavelet based features. In: Nachtegael, M., Van der Weken, D., Kerre, E.E., Philips, W. (Eds.), Wavelets and Fractals in Earth System Sciences. Springer, Berlin, Heidelberg, pp. 3–34.

Meyer, F., Agram, P., 2017. Modeling ionospheric phase noise for nisar mission data. In: 2017 IEEE International Geoscience and Remote Sensing Symposium, IEEE. https://doi.org/10.1109/IGARSS.2017.8127829.

Meyer, F.J., Nicoll, J.B., 2008. Prediction, detection, and correction of faraday rotation in full-polarimetric l-band sar data. IEEE Trans. Geosci. Remote Sens. 46, 3076–3086. https://doi.org/10.1109/TGRS.2008.2003002.

Münch, B., Trtik, P., Marone, F., Stampanoni, M., 2009. Stripe and ring artifact removal with combined wavelet fourier filtering. Opt. Exp. 17, 8567–8591. https://doi.org/10.1364/OE.17.008567.

Mohanty, S., Singh, G., 2019. Improved polsar model-based decomposition interpretation under scintillation conditions. IEEE Trans. Geosci. Remote Sens. 57, 7576–7578. https://doi.org/10.1109/TGRS.2019.2914171.

Mohanty, S., Singh, G., Carrano, C.S., Sripathi, S., 2018. Ionospheric scintillation observation using space-borne synthetic aperture radar data. Radio Sci. 53, 1187–1202. https://doi.org/10.1029/2017RS006424.

Moreira, A., Prats-Iraola, P., Younis, M., Krieger, G., Hajnsek, I., Papathanassiou, K., 2013. A tutorial on synthetic aperture radar. IEEE Geosci. Remote Sesn. Mag. 1, 6–43. https://doi.org/10.1109/MGRS.2013.2248301.

Ogden, T., 1997. Essential Wavelets for Statistical Applications and Data Analysis. Springer.

Pande-Chhetri, R., Abd-Elrahman, A., 2011. De-striping hyperspectral imagery using wavelet and adaptive frequency domain filtering. ISPRS J. Photogramm. Remote Sens. 66, 620–636. https://doi.org/10.1016/j.isprsjprs.2011.04.003.

Pi, X., 2015. Ionospheric effects on spaceborne synthetic aperture radar and a new capability of imaging the ionosphere from space. Space Weather 13, 737–741. https://doi.org/10.1002/2015SW001281.

Rakwatin, P., Takeuchi, W., Yasuoka, Y., 2007. Stripe noise reduction in modis data by combining histogram matching and facet filter. IEEE Trans. Geosci. Remote Sens. 45, 1844–1856. https://doi.org/10.1109/TGRS.2007.895841.

Ranchin, T., Wald, L., 1993. The wavelet transform for the analysis of remotely sensed images. Int. J. Remote Sens. 14, 615–619. https://doi.org/10.1080/01431169308904362.

Rogers, N.C., Quegan, S.R., Kim, J.S., Papathanassiou, K.P., 2014. Impacts of ionospherc scintillations on the biomass p-band satellite sar. IEEE Trans. Geosci. Remote Sens. 52, 1856–1868. https://doi.org/10.1109/TGRS.2013.2255880.

Roth, A.P., Huxtable, B.D., Chotoo, K., Chotoo, S.D., 2010. Simulating and mitigating ionospheric effects in synthetic aperture radar. In: 2010 IEEE International Geoscience and Remote Sensing Symposium, pp. 2892–2895. https://doi.org/10.1109/IGARSS.2010.5653180.

Roth, A.P., Huxtable, B.D., Chotoo, K., Chotoo, S.D., Caton, R.G., 2012. Detection and mitigation of ionospheric stripes in palsar data. In: 2012 IEEE International Geoscience and Remote Sensing Symposium, pp. 1621–1624. https://doi.org/10.1109/IGARSS.2012.6351218.

Sato, A., Yamaguchi, Y., Singh, G., Park, S., 2012. Four-component scattering power decomposition with extended volume scattering model. IEEE Geosci. Remote Sens. Lett. 9, 166–170. https://doi.org/10.1109/LGRS.2011.2162935.

Shimada, M., 2009. A new method for correcting scansar scalloping using forests and inter-scan banding employing dynamic filtering. IEEE Trans. Geosci. Remote Sens. 47, 3933–3942. https://doi.org/10.1109/TGRS.2009.2027596.

Shimada, M., Muraki, Y., Otsuka, Y., 2008. Discovery of Anoumoulous Stripes Over the Amazon by the PALSAR onboard ALOS satellite. In: 2008 IEEE International Geoscience and Remote Sensing Symposium, pp. II-387–II-390. https://doi.org/10.1109/IGARSS.2008.4779009.

Singh, G., Malik, R., Mohanty, S., Rathore, V., Yamada, K., Umemura, M., Yamaguchi, Y., 2019. Seven-component scattering power decomposition of polsar coherency matrix. IEEE Trans. Geosci. Remote Sens. Early Access. https://doi.org/10.1109/TGRS.2019.2920762.

Torres, J., Infante, S., 2001. Wavelet analysis for the elimination of striping noise in satellite images. Opt. Eng 40, 1309–1314. https://doi.org/10.1117/1.1383996.

vanZyl, J.J., Zebkar, H.A., Elachi, C., 1987. Imaging radar polarization signatures: Theory and observation. Radio Sci. 22, 529–543. https://doi.org/10.1029/RS022i004p00529.

Wang, H., Zhang, Y., Xu, J., Liao, G., Zhu, S., 2018. Range ambiguity suppression in a synthetic aperture radar using pulse phase coding and two-pulse cancellation. Int. J. Remote Sens. 39, 6525–6539. https://doi.org/10.1080/01431161.2018.1460509.

Watson, K., 1993. Processing remote sensing images using the 2-d fft–noise reduction and other applications. Geophysics 58, 780–916. https://doi.org/10.1190/1.1443468.

Wheelon, A.D., 2003. Electromagnetic scintillation. Vol. 2: Weak scattering. Cambridge University Press.

Yamaguchi, Y., Moriyama, T., Ishido, M., Yamada, H., 2005. Four-component scattering model for polarimetric sar image decomposition. IEEE Trans. Geosci. Remote Sens. 43, 1699–1706. https://doi.org/10.1109/TGRS.2005.852084.

Yang, J., Yamaguchi, Y., Lee, J.S., Touzi, R., Boerner, W.M., 2015. Applications of polarimetric SAR. J. Sensors 2015. https://doi.org/10.1155/2015/316391.